

New X-shaped bulge photometric model as a tool for measuring B/PS bulges and their X-structures in photometric studies

Anton A. Smirnov^{1,2*}, Sergey S. Savchenko^{1,3}

¹*St. Petersburg State University, Universitetskij pr. 28, 198504 St. Petersburg, Stary Peterhof, Russia*

²*Central (Pulkovo) Astronomical Observatory of RAS, Pulkovskoye Chaussee 65/1, 196140 St. Petersburg, Russia*

³*Special Astrophysical Observatory, Nizhniy Arkhыз, 369167 Karachai-Cherkessia, Russia*

Accepted XXX. Received YYY; in original form ZZZ

ABSTRACT

Recent orbital studies of 3D bar structure in various numerical and analytical models show that X-structures that reside in boxy/peanut-shaped (B/PS) bulges are not delineated by some specific type of orbits, but are natural parts of them and formed by the same orbits that constitute such bulges. This implies that to accurately account for B/PS bulges and their X-structures in photometric studies, one needs the photometric model of B/PS bulge that includes an X-structure as its natural part. To find such a model, we considered a self-consistent numerical galaxy model where a typical B/PS bulge arises. Using spectral characteristics of particle-“stars”, we decomposed the galaxy model onto the bar and non-bar components. We used the extracted 3D bar component to find an appropriate B/PS bulge photometric model, which can account for X-structures residing in such bulges. The resulted B/PS bulge photometric model has a truncated 2D Sersic profile with truncations introduced above (in the upper half-plane) and below (in the bottom half-plane) the rays of X-structures. We applied this model to represent B/PS bulges of various numerical models and some real galaxies. The comparison with previous works revealed that there are systematic shifts between the X-structure parameters of the same galaxies measured within the different approaches. We found that the geometric parameters of X-structures of real and modelled galaxies are consistent with each other if we measure them using our new model.

Key words: galaxies: bulges – galaxies: bar – galaxies: photometry – galaxies: structure.

1 INTRODUCTION

X-structures are cross-shaped structures observed in some disk galaxies seen edge-on. The classic example of the galaxy with such a peculiar morphology is NGC 128. The central area of this galaxy has a peanut-like profile. A careful observer can identify four thick lobes protruding from the disc plane and distinguishable on the background of the peanut. These lobes are almost symmetric with respect to the disc plane, and they are connected to the very central area of the galaxy. Such structures frequently referred as an X-shape or an X-structure. The whole peanut-like structure (including X-structure) is usually referred as a peanut bulge. In some galaxies (for example, NGC 7332) the bulges of a similar physical nature appear in a form of the box. The common wisdom is to refer to the whole set of such objects as boxy/peanut-shaped (B/PS) bulges.

Studies of B/PS bulges in disc galaxies have a rather long history. First seminal work where such bulges were distinguished was done in the late fifties by [Burbidge & Burbidge \(1959\)](#).

Authors considered three galaxies one of which was mentioned above NGC 128. In this work one can also find the first implicit reference to the X-structure inhabiting this galaxy: “*At the widest parts of the nuclear region there are four bulges of about equal size, coming out of the nucleus itself like a cross.*” ([Burbidge & Burbidge 1959](#)). The term ‘X-shape’ itself was introduced later on in the study of IC 4767 galaxy by [Whitmore & Bell \(1988\)](#). The isophotes in the central part of this galaxy show a typical peanut profile. The ‘X-shape’ itself was revealed after subtracting the disc model from the original image of the galaxy.

More recent works ([Jarvis 1986](#); [Shaw 1987](#); [de Souza & Dos Anjos 1987](#); [Lütticke et al. 2000](#); [Erwin & Debattista 2013](#); [Yoshino & Yamauchi 2015](#); [Erwin & Debattista 2017](#); [Kruk et al. 2019](#)) show the fraction of disc galaxies with B/PS bulges is quite significant. The fraction varies from 20%-25% ([Shaw 1987](#); [de Souza & Dos Anjos 1987](#); [Yoshino & Yamauchi 2015](#)) to 40% ([Lütticke et al. 2000](#)) for different samples. [Kruk et al. \(2019\)](#) tried to account for the projection effects and obtained that 70% of disc galaxies should possess B/PS bulges to the epoch $z = 0$ (present day). These studies generally show that B/PS bulges are quite common inhabitants of disc galaxies.

* E-mail: zeleniikot@gmail.com

Historically, there were different hypotheses concerning the physical nature of B/PS bulges and X-structures. Among them are the collapse of the protogalactic cloud (Jarvis 1981), the galaxy merging (Hernquist & Quinn 1988) and the accretion of the material during tidal encounters (Schweizer & Seitzer 1988). Although not completely (Binney & Petrou 1985), these theories mainly came to halt with the work of Combes & Sanders (1981) where the authors showed that the bars thickened in the vertical direction take the form of a peanut or a box depending on the angle between the bar major axis and the observer line of sight (LoS), $\approx 90^\circ$ for a peanut to be observed and generally less than 50° for a box to be observed, respectively¹. Further numerical studies reinforced these results (Combes & Sanders 1981; Combes et al. 1990; Friedli & Pfenniger 1990; Raha et al. 1991; Pfenniger & Friedli 1991). Subsequent kinematic studies of stars and ionised gas showed that B/PS bulges rotate cylindrically (Bertola & Capaccioli 1977; Kormendy & Illingworth 1982) and have a specific shape of LoS velocity distribution that arising due to bars residing in the observed galaxies (Kuijken & Merrifield 1995; Bureau & Freeman 1999; Merrifield & Kuijken 1999; Veilleux et al. 1999; Chung & Bureau 2004). These facts also supported the idea that B/PS bulges are just thickened bars. Recent studies have established a more accurate relationship between the B/PS bulges and their bars. Laurikainen et al. (2014); Athanassoula et al. (2015) showed that the so-called “barlenses” (near-circular central parts of the bars found in some face-on galaxies) seem to be the manifestations of the B/PS bulges when the latter viewed from near face-on orientations. Laurikainen & Salo (2017) provided evidence for the existence of such a link by a systematic study of how B/PS bulges and barlenses metric properties vary as a function of viewing inclination both in real and modelled galaxies.

The detailed reasons for bars to thicken are still the subject of debates. There are three possible physical mechanisms including instability of hose-pipe type (Raha et al. 1991), the resonance trapping of individual orbits (Quillen 2002), and so-called resonance heating (Quillen et al. 2014). The latter two are similar in a sense that the basic agent that forces stars to jump out from the disc plane is 2:1 vertical inner Lindblad resonance (vILR). Stars at the resonance experience non-zero net effect from the oscillating bar potential. They gradually accumulate small changes in momentum and sooner or later are forced to jump out of the disc plane. The actual distinction between trapping and heating is that the heating model is trying to account for the bar slow down (Athanassoula 2005) that leads to a change of the vILR location. The hose-pipe instability is associated with the bending waves. They become unstable if there is no sufficient ratio of vertical to radial velocity dispersion, σ_z/σ_R , to prevent the waves growth (Toomre 1966; Poliachenko & Shukhman 1977; Araki 1985; Merritt & Sellwood 1994). An interesting result concerning the mechanisms was obtained by Pfenniger & Friedli (1991). The authors run the experiments with forced vertical symmetry and showed that the peanut still forms, but on longer time scales. This result supports the idea that both the resonance trapping and bending waves are important for the growth of the peanut (see also recent work by Sellwood & Gerhard 2020).

The physical nature of the X-structures themselves is also an open question, although significant progress has already been made in this direction. The spatial resolution of the models was

not very good in the first numerical studies of 3D bar structure ($\approx 10^3 - 10^4$ particles represented the disc component). X-structures were only distinguished in unsharp masked images constructed from such models. Some authors (Friedli & Pfenniger 1990; Pfenniger & Friedli 1991) therefore suggested that X-structures are akin to an optical illusion due to the tendency of eyes to perceive the intensity gradients instead of actual intensity values. However, with an increase of spatial resolution, it became evident that the X-structures are real density enhancements that can be observed even without unsharp masking processing (see Smirnov & Sotnikova (2018) for many representative examples). The question then is why such density enhancements are observed. Studies of orbit composition of B/PS bulges and X-structures in different numerical and analytical models (Patsis et al. 2002; Quillen 2002; Patsis & Katsanikas 2014a; Quillen et al. 2014; Parul et al. 2020) showed that an X-shape is observed in these models due to a tendency of a star to spend more time near turning points of its trajectory. More specifically, 3D bars are constituted by different types of periodic, quasi-periodic, and sticky chaotic orbits (Pfenniger 1984; Pfenniger & Friedli 1991; Skokos et al. 2002; Patsis et al. 2002; Patsis & Katsanikas 2014a,b; Patsis & Harsoula 2018; Patsis & Athanassoula 2019). Stars that move along such orbits spend different periods of time in different parts of their trajectories. For example, stars moving along banana-shaped orbits (Pfenniger & Friedli 1991) spend more time at the highest points of their trajectory (Patsis et al. 2002; Patsis & Katsanikas 2014a). Therefore, the bulk of such orbits produces a density profile with visible density enhancements at the highest points of such orbits. For an X-structure to be observed, these density enhancements should be aligned along an almost straight line for orbits with different apocentric distances. This is indeed the case for the realistic bar potential (Patsis et al. 2002; Quillen 2002; Patsis & Katsanikas 2014a; Quillen et al. 2014). Parul et al. (2020) showed that the orbits of a more complicated morphology than banana-shaped orbits can build an X-structure in a similar manner. In general, cited works showed that X-structures and B/PS bulges are produced by the same orbits. They are not constituted by different types of orbits like, for example, disc and classical bulge components. The open question that has to be answered in the upcoming studies is what types of orbits are actually presented in real galaxies.

An important aspect of the physical nature of B/PS bulges (and their X-structures) is that they are products of a secular evolution of the host galaxy. Consequently, the physical properties of these components should be tightly connected with the properties of the underlying gravitational potential. This includes the potential imposed by the dark matter component (Smirnov & Sotnikova 2018). Therefore, the detailed observational studies of B/PS bulges and X-structures can provide additional important constraints on the dynamics of the galaxies that host such objects.

The most promising candidates for such studies are galaxies seen edge-on. In such galaxies, one can try to assess not only the sizes of the B/PS bulges (which can be done in intermediate inclined galaxies, see Erwin & Debattista 2013) but characterise the shape of the B/PS bulges (Ciambur & Graham 2016) and characterise their most prominent features - X-structures (Laurikainen & Salo 2017; Savchenko et al. 2017). An important thing to stress out here is that all groups of authors used different processing algorithms. Ciambur & Graham (2016) quantified B/PS bulges as a whole (including X-structures) fitting isophotes by a Fourier modified ellipses, while Laurikainen & Salo (2017); Savchenko et al. (2017) studied only the X-structures using

¹ It is difficult to determine a strict value of the angle in the general case since it depends on the size of the peanut itself.

unsharp-masking and photometric decomposition, respectively. The difference in approaches gives rise to some inconsistency in results obtained in these works. The most clear example is ESO 443-042 galaxy. Ciambur & Graham (2016) obtained that an X-structure residing in this galaxy is very flattened (their horizontal and vertical sizes are 20.0 arcsec and 5.1 arcsec, respectively, see their table 2), while the X-structure extracted by Laurikainen & Salo (2017) seems quite typical (horizontal and vertical sizes 15.7 arcsec and 12.0 arcsec, respectively, see their table F.2).

In our previous work where we considered a rather large set of different numerical models Smirnov & Sotnikova (2018) we obtained that modelled X-structures seem to be less flattened than real observed X-structures. We characterised the flatness of X-structure in terms of the value of the angle between the disc plane and the ray of an X-structure. X-structures in our models demonstrated opening angles between 26° and 42° , while the opening angles of real X-structures have values in nearly the same range with a slight shift to the lower values (Savchenko et al. 2017). This is disturbing because the opening angles observed in real galaxies actually should be shifted to the greater values than 30° due to the projection effects (see figure 22 in Smirnov & Sotnikova (2018)). In principle, such inconsistency can also arise due to slightly different approaches to measuring X-structure opening angles in Smirnov & Sotnikova (2018) and Savchenko et al. (2017). In Savchenko et al. (2017) the density maxima were measured along photometric cuts perpendicular to the rays of X-structure while in Smirnov & Sotnikova (2018) we used cuts parallel to the disc plane. However, this should be strictly verified because there are exist some physical reasons why the observed X-structures can appear more flattened. For example, X-structures flatten in course of their secular evolution (Smirnov & Sotnikova 2018). Therefore, a large flatness of observed X-structures can be an indicator that they live on average longer than 6-8 Gyrs (Smirnov & Sotnikova 2018). Strongly flattened X-structures can be also observed in galaxies with a large contribution of dark matter within the optical radius of the disc Smirnov & Sotnikova (2018).

One more inconsistency between Smirnov & Sotnikova (2018) and Savchenko et al. (2017) is that X-structures extracted by Savchenko et al. (2017) usually show curved rays (see figure 4 there) which is not the case for X-structures from numerical models. Again, this can be an indicator that there are a mix of orbital families which support B/PS bulge in observed galaxies (Patsis & Harsoula 2018; Parul et al. 2020) or the effect due to the difference in processing algorithms.

In the present work, we would like to specifically address the question of whether or not the mentioned inconsistencies are due to the difference in processing algorithms or a real physical effect. To this aim we apply exactly the same methods of B/PS bulges analysis for some numerical models from Smirnov & Sotnikova (2018) and real galaxies from the samples considered by Ciambur & Graham (2016) and Savchenko et al. (2017). We note that the idea to study the B/PS bulges of numerical models and real galaxies using the same processing algorithms has already been exploited by Laurikainen & Salo (2017) and allowed the authors to obtain important results concerning B/PS bulges – barlenses connection, thus proving to be quite fruitful.

We choose to work within the framework of photometric decomposition as it was done in (Savchenko et al. 2017). But unlike the photometric model for the X-structure considered in Savchenko et al. (2017), we tried to construct a new photometric model which accounts simultaneously for both B/PS bulge and its X-structure. Such an approach is more consistent with

recent studies of X-structures and B/PS bulges where authors showed that the X-structures are inextricable parts of the B/PS bulges (Patsis et al. 2002; Patsis & Katsanikas 2014a; Parul et al. 2020). We deduced the new photometric model on the basis of “dynamical” decomposition of a numerical model of a Milky Way-like galaxy from Smirnov & Sotnikova (2018). The “dynamical” decomposition is the decomposition of the galaxy onto different orbital groups or families based on the orbital frequencies. This decomposition was done using the methods of spectral dynamics (Binney & Spergel 1982) as it was done in Parul et al. (2020).

The manuscript has the following structure. In Section 2 we present our new photometric model. In Section 3 we give the details of the fitting procedure. In Section 4 we study how the new B/PS bulge photometric model changes its parameters depending on other photometric components (disc, classical bulge), as well as projection effects (disc inclination angle, bar azimuthal viewing angle), and also consider some important trends arising due to the difference in the physical parameters of the modelled galaxies. In Section 5 we describe our sample of real galaxies and show a few examples how the new photometric model works in case of real galaxies. In Section 6 we compare our results for full galaxy sample with results of previous works, and verify whether different measuring techniques give the same results on the same galaxies. In Section 7 we compare B/PS bulge geometric parameters of real galaxies with those of some numerical models. In Section 8 we summarise our results.

2 PHOTOMETRIC MODEL OF THE X-SHAPED BULGE

B/PS bulges are usually described by a Sersic function (Sersic 1968),

$$I(x, y) = I_e \exp \left[-v_n \left(\left(\frac{r}{r_e} \right)^{1/n} - 1 \right) \right], \quad (1)$$

where I_e is the effective brightness, r_e – the effective radius, n – the Sersic index, v_n is a function depending on n (Caon et al. 1993) and r corresponds to major axis of the ellipse with ellipticity ϵ that passes through the point with coordinates (x, y) , or Ferrers function (Ferrers 1877),

$$I(r) = I_0 \left[1 - \left(\frac{r}{r_{\text{out}}} \right)^{2-\beta} \right]^\gamma, \quad r < r_{\text{out}} \quad (2)$$

where I_0 is the central intensity, r_{out} is the truncation radius, β and γ control the overall shape of the profile, and r is the same isohotal radius as in Eq. (1). Both functions lack the ability to account for the X-shaped structures in real galaxies because of their symmetries. This is a crucial problem if we want to measure the X-structure parameters in the framework of the photometric decomposition. Savchenko et al. (2017) solved this problem by adding the Fourier distortion to the Ferrers profile (2) in the following form:

$$r = r_0 [1 + a_4 \cos(4(\varphi + \varphi_0))], \quad (3)$$

where a_4 and φ_0 are the amplitude and phase of Fourier distortion, respectively. Right part of Eq. (3) is meant to be inserted in Eq. (2) instead of r variable thus obtaining the profile with four symmetric lobes. The photometric model obtained in this way can indeed describe the B/PS bulge and its X-structures, but rather not convenient for measuring the parameters of X-structures. For example, to obtain the opening angle value, one needs to perform

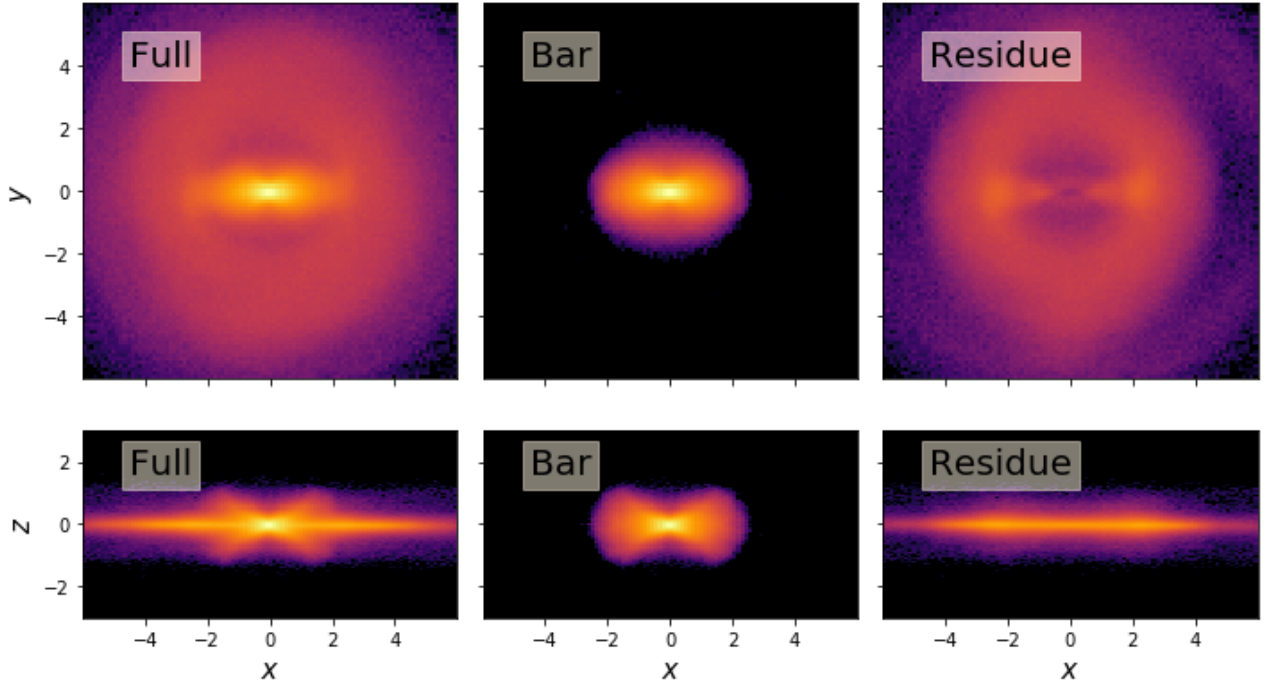


Figure 1. The decomposition of the galaxy model (*left column*) on the bar part (*mid column*) and the residue part (*right column*) by means of the frequency analysis.

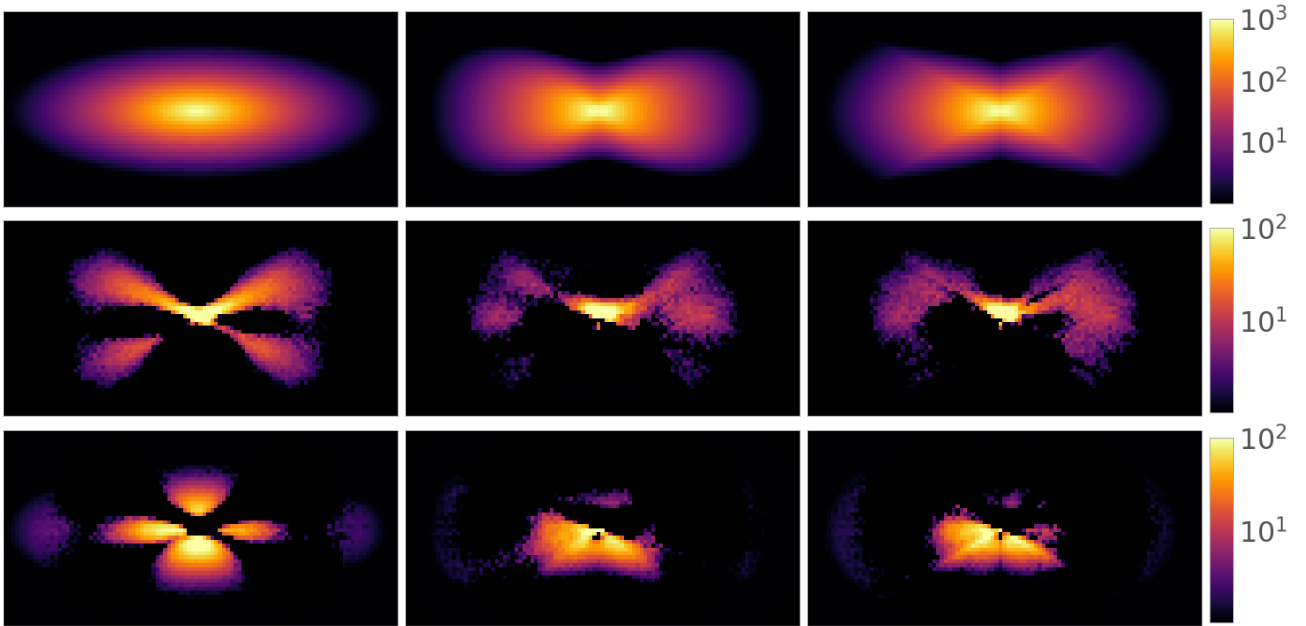


Figure 2. Different photometric models of the vertical bar distribution shown in Fig. 1 (*upper row*) and the residue images, the positive part (*middle row*) and the negative part (*bottom row*). *Left column*: Sersic profile; *Middle column*: model from Savchenko et al. (2017); *Right column*: the photometric model from the present work.

an additional round of measurements using the photometric cuts as it was done in Savchenko et al. (2017). There is also a problem with photometric cuts that the result can depend on whether one uses cuts parallel to the disc plane or at some specific inclination to the plane. Here we want to avoid this problem and characterise B/PS bulges and their X-structures only employing an appropriate

photometric model. To this aim, we construct a new photometric model in which the value of the opening angle is set explicitly.

Let us consider the bar and the corresponding B/PS bulge in some typical galaxy model where the bar naturally arises due to effects of the self-gravity (precise details of the simulation will be given in the next section). Fig. 1 shows the density distributions in both (xy) and (xz) planes produced by all particles representing

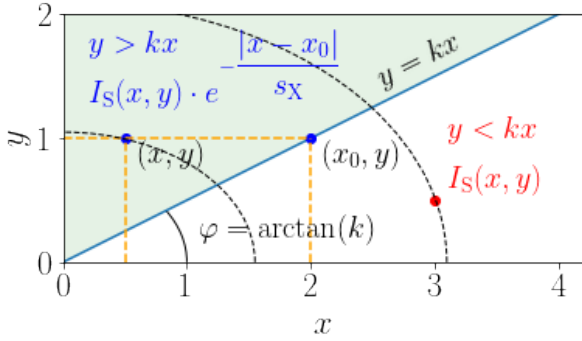


Figure 3. Schematic image showing how the intensity is calculated in the X-shaped bulge photometric model defined by Eq. (5). I_S stands for the intensity calculated for a non-modified Sersic function.

the stellar component (*left column*), bar particles (*middle column*) and all particles that are not the bar particles (*right column*) in the model after 6 Gyr of evolution. The presented division on the bar and not bar components was done using the spectral characteristics of the orbits, f_R/f_x and f_z/f_x frequency ratios and the values of f_x and f_y frequencies themselves, where x, y, z are coordinates in the reference frame co-rotating with the bar, R — the cylindrical radius and f_x, f_y, f_z , and f_R are the frequencies of oscillations along the corresponding axes. The bar particles was identified as the particles that have $f_R/f_x < 4$, $f_z/f_x < 2.1$ and $f_x \gtrsim 21 \text{ km s}^{-1} \text{ kpc}^{-1}$ and $f_y \gtrsim 21 \text{ km s}^{-1} \text{ kpc}^{-1}$. Analogous division was done in Parul et al. (2020) and a similar approach was also used to distinguish the bar by several authors before that (Ceverino & Klypin 2007; Portail et al. 2015; Gajda et al. 2016). Here we stray from the “typical” frequency ratio condition $f_R/f_x = 2 \pm 0.1$ used in the previous works, because we found it to be insufficient to accurately extract the bar in this model. Since the bar shown in Fig. 1 is cleared from the disc contribution (and also ansae, see the right column of Fig. 1) this makes it an ideal target for studying how well various photometric models represent the actual bar density profile. This is an advantage of the galaxy models laying in the fact that we can avoid the need to account for other components and study only the density distribution of the B/PS bulge itself.

Fig. 2 shows three different best-fit models of the bar density distribution from Fig. 1: pure Sersic model (*left column*), model from Savchenko et al. (2017) (*middle column*) and our new photometric model (*right column*), details of which will be given below. The fitting procedure was done using IMFIT package (Erwin 2015). To find the optimal values of parameters, we used Gaussian-based maximum likelihood statistic which is the total χ^2 for the model:

$$-2 \ln \mathcal{L} = \chi^2 = \sum_{i=0}^N w_i (I_{m,i} - I_{d,i})^2, \quad (4)$$

where w_i are the pixel weights and $I_{m,i}$ and $I_{d,i}$ are intensities of the individual pixels in the photometric model and in the image which we try to fit, respectively. Hereandafter we give the chi-square values normalised to the degrees-of-freedom $\nu = n - m$, where n is the number of unmasked pixels and m is the number of free parameters. The Sersic model is given in Fig. 2 mostly for methodological purposes. It just shows that the usual Sersic model applied to the bar gives four bright rays in the residue images, which we then call X-structures. The model of Savchenko et al. (2017) is good at capturing the overall behaviour of the intensity

profile but does not have the sharp rays, the parameters of which we can associate with the parameters of X-structures. To construct a more practical photometric model in which the value of the opening angle would be an explicit parameter of the model, we considered a Sersic profile (1) and add the truncation to it in the following form:

$$I(x, y) = \begin{cases} I_S(x, y), & y \leq kx, \\ I_S(x, y) \cdot \exp(-|x - x_0|/s_x), & y > kx. \end{cases} \quad (5)$$

Here $I_S(x, y)$ stands for the Sersic intensity profile defined in Eq. (1), x and y are the pixel coordinates, k is an angular coefficient of the X-structure ray which translates into the opening angle value $\varphi = \arctan k$, x_0 is the abscissa of the point that has an ordinate y but belongs to the X-structure ray, $x_0 = y/k$, and s_x is the parameter that determines how fast the intensity is declining above the ray. Eq. (5) is written for the first quadrant but easily translates for other three with appropriate change of signs before x and y . Fig. 3 schematically shows how the intensity is calculated in such a model. The profile below the ray is identical to the pure Sersic brightness distribution. The brightness above the ray decreases compared to values given by the Sersic’s law as we move away from the ray. We experimented with different laws of density declining. For example, we also considered a Gaussian type of declining but found that the Gaussian type and the exponential type produces nearly the same results. We have chosen the exponential law as one of the simplest. We also note the horizontal direction of the density declining in Eq. (5) is the result of some trial and error. We also considered density declining along the elliptical isophotes and a straight line perpendicular to the ray of the X-structure. In both of these cases, we found that such models produce some unrealistic X-shaped bulges when applied to our sample of real galaxies.

One of the important parameters that our model inherits from the Sersic function is an ellipticity of the isophotes ϵ . But in contrast to the simple Sersic model, the ellipticity parameter in this new model characterises only that part of the isophotes that is below the ray of X-structure, while the shape of isophotes above the ray is determined both by ellipticity and s_x parameter. For technical reasons, we define the ellipticity in the following way:

$$\epsilon = \begin{cases} 1 - b/a, & b \leq a \\ a/b - 1, & b > a, \end{cases} \quad (6)$$

where a and b are the major and minor axes lengths of the given isophote, respectively. According to Eq. (6), ϵ can take values from -1 to 1 , or, in other words, we allow the model to have prolate isophotes between the disc plane and the rays of X-structure.

The photometric model from Savchenko et al. (2017) is almost identical to our photometric model (5) in terms of the statistic value per pixel and even slightly better, 0.7 versus 0.8, respectively. Although both of them are a significant improvement over the Sersic model with a statistic value of 1.8. The residue images also look similar (Fig. 3). To our surprise, the residues show clear asymmetries at the level about 10% of the total intensity (see colorbar annotation). Probably, such asymmetries are remnants of the buckling event in this particular galaxy model. It is also interesting that the model from Savchenko et al. (2017) applied to the pure bar does not show the dark blobs between the rays of X-structure that are observed in almost all of Savchenko et al. (2017)’s X-structure images for real galaxies. Perhaps this means that the blobs are not due to the bulge model, but due to their disc model.

Our new photometric model is characterised by nine different

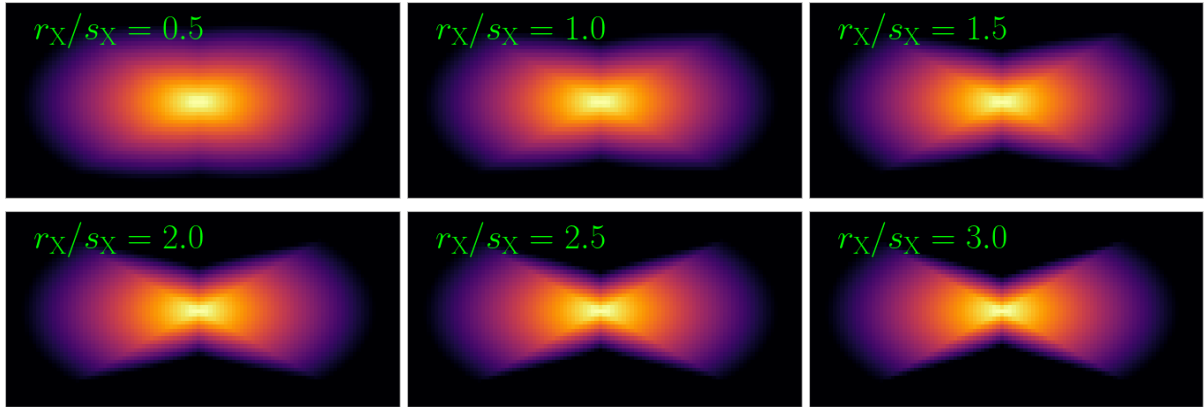


Figure 4. Examples of the X-shaped bulge model appearance for different values of the sharpness parameter r_X/s_X and the fixed effective length r_X , the Sersic index $n_X = 1$, and the opening angle $\varphi = 30^\circ$. The other parameters are the same for all cases .

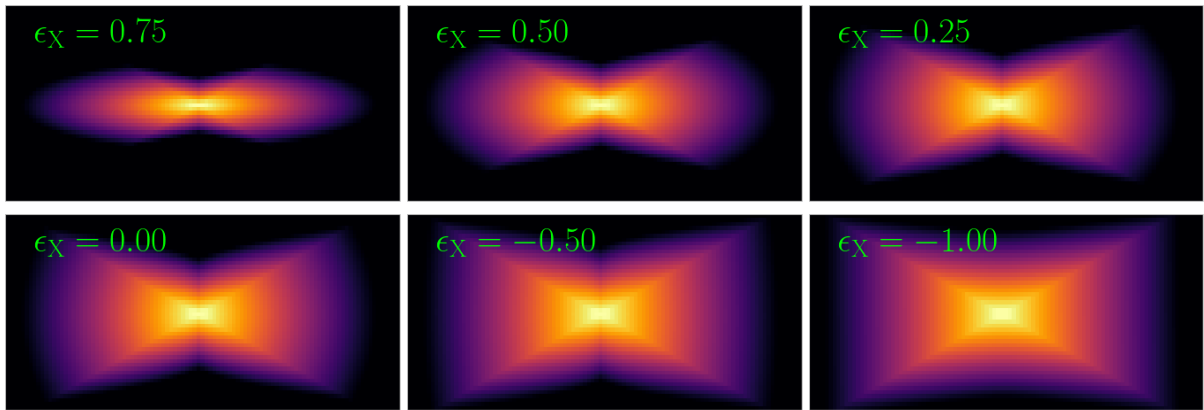


Figure 5. Examples of the X-shaped bulge model appearance for different values of the ellipticity ϵ_X and the fixed values of the sharpness parameter $r_X/s_X = 2$, the Sersic index $n_X = 1$, and the opening angle $\varphi = 30^\circ$. The other parameters are the same for all cases.

parameters in total. Four of them are common parameters of any component, such as the coordinates of the centre, the positional angle of the component, and the central intensity. The other three are inherited from the Sersic model. These are the effective radius of the Sersic profile r_X , the Sersic index n_X and the ellipticity of the isophotes below the rays ϵ_X . Here we have added a subscript to avoid further confusion with a simple Sersic model. The other two parameters are specific for this particular model and include the opening angle of the X-structure ray φ , and the scale length s_X , which characterises the density dip above the ray. In practise, we found that the ratio r_X/s_X is a good indicator of how pronounced the X-structure we observe. In Fig. 4 we give several examples of the model appearance for different values of this parameter. It can be seen that the lower its value, the smaller the density dip between the rays, and the closer our model is to the usual Sersic model. For shortness, we call this parameter the sharpness parameter in further discussion. In principle, one can associate the value of this parameter with the shape of the B/PS bulge to indicate if it has a rather boxy shape or peanut-like shape. However, the ellipticity ϵ_X also affects the intensity profile above the ray. This is due to the fact that we truncate the intensity of a Sersic photometric model that has elliptical isophotes on its own. In Fig. 5 we show how the model changes with ellipticity ϵ_X for a fixed value of r_X/s_X . It is clearly seen that the overall shape of the profile becomes more boxy-like with a decrease in ϵ_X . At the same time, we observe a

prominent X-structure in all cases. The figure shows that the degree of boxyness can be strictly compared only among the models with similar values of r_X/s_X . The pleasant side of a such rather complex behaviour is that the model can account for cases when we observe a boxy-shaped bulge but with a prominent X-shape on top of it.

Concluding this section, we obtained the photometric model of the B/PS bulge, at which the X-structure opening angle value is set explicitly. Since the model now has four explicit rays, it is more accurate to call it “the X-shaped bulge model” (or XB model for short) rather than the B/PS bulge model. To be definite, we will refer to our model in this way.

3 THE FITTING STRATEGY

Since our photometric model has two more parameters than the usual Sersic bulge model the fitting of the model requires some additional care. In this section, we describe how we approached this problem. First of all, we assume that the Sersic index n_X for the X-shaped bulge should be close to one. This assumption is based on the fact that the bars were once part of the discs in which they reside and usually have a density profile of exponential type. Therefore, we work with a fixed value of the Sersic index $n_X = 1$ for both real and modelled galaxies. For safety, we performed additional runs with a free value of n_X for some of the simulated galaxies and found

that it is indeed close to one for various models (from about 0.9 to 1.3, more precisely).

The fitting itself was performed in an iterative manner to let us move from a simple initial to a complex final model. We divided the whole procedure into three stages, namely:

(i) preliminary run; the purpose of this run is to determine the appropriate initial conditions for the X-shaped bulge model.

(ii) auxiliary run; this run softens the transition between the preliminary run and the final runs.

(iii) final run; the final run consists of the actual fitting of the X-shaped bulge model along with other photometric components.

The details of the runs are as follows. During the preliminary run we find the best-fit photometric model of the galaxy by fitting B/PS bulge by the pure Sersic function with a fixed Sersic index value, $n = 1$, and a fixed value of the positional angle (PA), $\varphi_{\text{PA}} = 90^\circ$. At this stage, we do not use our X-shaped bulge model yet. The fitting is done along with other components such as disc, ring, etc. After we obtained the optimal parameters of the pure Sersic bulge, we construct the initial conditions for the X-shaped bulge model based on the pure Sersic bulge parameters. Here we should choose values for only two additional parameters, φ and s_X . All others can be directly taken from the previously obtained pure Sersic model. The characteristic range of the opening angles of real galaxies is from 20° to 40° . The value of the opening angle can be chosen pretty safely near 30° then. The scale length s_X can be estimated in different ways but we choose to equate it to the characteristic vertical scale length of the disc component z_d . When we obtained the initial set of the parameters for the X-shaped bulge photometric model, we again perform the photometric fitting of all components from the preliminary run now with the X-shaped bulge model. However, we do not free all the parameters of the X-shaped bulge at once. We first perform the auxiliary run fitting the X-shaped bulge with a fixed value of PA, $\varphi_{\text{PA}} = 90^\circ$, and fixed coordinates of its centre. At this step, we can also introduce some additional components such as a ring or a small Gaussian. Finally, we free all the parameters of the X-shaped bulge model except for the Sersic index n_X , which remains equal to one till the end, and again perform the fitting. This is the final run.

Another specific aspect of our research is that we consider a rather unusual disc model. We consider a model of the so-called anti-truncated disc (AT disc hereinafter) which is characterised by the presence of the hole in its centre:

$$j(r, z) = j_0 \operatorname{sech}^{2/n} \left(\frac{nz}{2z_0} \right) \times \begin{cases} \exp \left(-\frac{r}{h} \right), & r \geq R_T, \\ \exp \left(-\frac{r}{h} - \frac{R_T - r}{h_T} \right), & r < R_T. \end{cases} \quad (7)$$

Here j_0 is the central luminosity density, h is the exponential scale length in the disc plane, z_0 is the vertical scale height, n determines to which type of profile the vertical distribution is closer, sech^2 with $n = 1$ or $\exp(-z/z_d)$ with $n \rightarrow \infty$, R_T is the size of the hole and h_T is the characteristic scale length of the density decrease towards the centre. Eq. (7) is written in a cylindrical coordinate system (r, z) . The actual intensity in the given pixel is obtained by integrating $j(r, z)$ along a LoS.

The reasons to consider AT discs in this study are the following. In general, AT discs are frequently discussed in context of bars although not all bars reside in such discs and not all AT discs owe their existence to bars (see, for example, Kim et al. (2014) and

references therein)². However, the discs in our models indeed have apparent AT profile if seen face-on (see Fig. 1). The problem then if we decompose a galaxy applying a simple exponential disc model while the disc actually has a hole in the centre we distort B/PS bulge profile in some non-trivial way. If we then apply AT disc model the distortion effect should be compensated at least partially (at least it is reasonable to assume so). We discuss the matter of different disc models more thoroughly in the next subsection considering the decomposition of a particular numerical model. The fitting of the AT disc model is not that simple itself. In practice, we found that there are some cases when it is necessary to assign some reasonable values to the hole parameters R_T and h_T and fix them until we find a rough approximation of the X-shaped bulge model in the preliminary run. We free them only in the final run.

Other photometric components we use are quite typical for studies of this kind. We use a Gaussian ring, luminosity density of which is determined by the following expression:

$$j(r, z) = j(r_{\text{ring}}, 0) \exp \left(-\frac{(r - r_{\text{ring}})^2}{2\sigma_{\text{ring}}^2} \right) \exp \left(-\frac{|z|}{h_z} \right), \quad (8)$$

where r_{ring} is the ring radius, σ_{ring} is the ring width, h_z is the scale height and $j(r_{\text{ring}}, 0)$ is the luminosity density at $r = r_{\text{ring}}$. In some cases we also use simple Gaussian:

$$I(a) = I_0 \exp(-a^2/(2\sigma^2)). \quad (9)$$

Here σ is the characteristic size and a is the distance between the given pixel and the Gaussian centre. To account for the dust in real galaxies we use the same method as in Savchenko et al. (2017). We represent the dust component by an edge-on disc with the negative intensity. The edge-on disc intensity is calculated using the following expression:

$$I(r, z) = \mu(0, 0) \frac{r}{h} K_1 \left(\frac{r}{h} \right) \operatorname{sech}^{2/n} \left(\frac{nz}{2z_0} \right), \quad (10)$$

where $\mu(0, 0)$ is the central surface brightness, K_1 is the modified Bessel function of the first kind and all other notations are the same as in Eq. (7).

To estimate uncertainties of the parameters we use bootstrap resampling available in IMFIT package. We performed 200 iterations for each of the fits as recommended by the IMFIT author.

Below we present results obtained from the decomposition of models and real galaxies. We start with numerical models and show how various effects that are intrinsically non-physical (like projection effects, which include both possible disc inclination and the rotation of the bar around the disc axis) and the effects that associated with the choice of photometric model (in particular, the disc model) affect the output parameters of B/PS bulges. We also investigate the behaviour of a particular model with a classical bulge to check how the presence of a bulge of another physical nature affect the measured B/PS bulge parameters. Then we compare the parameters obtained from the physically different models and finally compare the latter with those obtained from the decomposition of real galaxies.

Table 1. Parameters of models

$M_h(R < 4R_d)/M_d$	z_d/R_d	$Q(2R_d)$	M_b	r_b	$N_d, 10^6$	$N_h, 10^6$	$\varepsilon_d/R_d, 10^{-3}$	$\varepsilon_h/R_d, 10^{-3}$
1.5	0.05	1.2	0	-	4	4.5	3.68	12.8
1.5	0.05	1.2	0.2	0.2	4	4.5	3.68	12.8
1.5	0.05	1.6	0	-	4	4.5	3.68	12.8
3.0	0.05	1.2	0	-	4	9	3.68	10.2

Notes: each column represents parameters of the models, one model per line. $M_h(R < 4R_d)$ is the mass of the halo within a sphere with a radius of $4R_d$, where R_d is the scale length of the disc, M_d is the total disc mass, z_d/R_d is the initial ratio of the disc scale height to the disc scale length, $Q(2R_d)$ is the value of the Toomre parameter at $2R_d$, M_b and r_b are the total mass and the scale length of the bulge, respectively. N_d and N_h are the numbers of particles in the disc and the halo, respectively, and ε_d and ε_h are the softening lengths of the disc and halo particles, respectively.

4 NUMERICAL MODELS

In the present work we consider four different galaxy models from Smirnov & Sotnikova (2018). Full details of the simulations can be found in that work and we refer an interested reader to it. Here we briefly describe some important aspects of the simulations. Initially, each model consists of an axisymmetric exponential disc

$$\rho(R, z) = \frac{M_d}{4\pi R_d^2 z_d} \exp\left(-\frac{R}{R_d}\right) \operatorname{sech}^2\left(\frac{z}{z_d}\right), \quad (11)$$

where M_d is the total mass of the disc, R_d is the disc scale length and z_d is the disc scale height, plus spherically symmetric dark halo of NFW-type (Navarro et al. 1996). The halo is characterised by the ratio $M_h(r < 4R_d)/M_d$, where $M_h(r < 4R_d)$ is the dark halo mass inside the sphere with a radius of $4R_d$. One model also includes a Hernquist type bulge (Hernquist 1990):

$$\rho_b(r) = \frac{M_b r_b}{2\pi r (r_b + r)^3}, \quad (12)$$

where r_b is the scale parameter and M_b is the total bulge mass. Disc and halo components are represented by several millions of particles (see Tab. 1). Bulge particle number is chosen such that the mass of one particle from the bulge is equal to the mass of one particle from the disc. Some important physical parameters of the models are specified in Tab. 1. The initial equilibrium state of each multi-component model was prepared via script `mkgalaxy` (McMillan & Dehnen 2007) from the toolbox for N-body simulation NEMO (Teuben 1995). Evolution of the models was followed for about 8 Gyr using the fastest N-body code for one CPU `gyrfalcon` (Dehnen 2002). Each model gives rise to a bar after 1 – 2 Gyr from the beginning of the simulation. Each bar gradually thickens in the vertical direction (clear buckling events can occur depending on the model) and takes a B/PS shape if seen side-on. Fig. 1 shows the end-state of the bulgeless model with $\mu = 1.5$ and $Q(2R_d) = 1.2$. This model is our fiducial or “main” model. On the example of this model, we consider below how various projection effects affect the extracted parameters of the B/PS bulge. For each of the models, we prepared a set of FITS images obtained from the corresponding density distribution of disc/bulge particles. Such images can then be decomposed using

a usual decomposition procedure analogous to that used for images of real galaxies.

4.1 Results for numerical models

Most of the results presented in this subsection concern various non-physical effects like projection effects or the impact of different photometric models of the disc on the X-shaped bulge parameters. To analyse such effects, we use our “main” model and choose a specific time moment, namely $T \approx 6$ Gyr after the beginning of the simulation. To this moment, the buckling events have already passed and the B/PS bulge evolves only slowly, with almost no changes in the X-structure morphology. Using the stellar component density distribution for this moment, we prepared a set of FITS images for various orientations of the bar with respect to the disc axis (bar azimuthal angle) and various inclinations of the disc plane. The bar angle is calculated from LoS, that is, the angle is 0° when the bar major axis is aligned along LoS and 90° when the bar major axis is orthogonal to LoS.

While our X-shaped bulge photometric model in principle is characterised by nine different parameters only four of them are of interest for comparison with real observational data. The fact is that the value of any dimensional quantity (size, intensity) measured from models depends on our normalisation procedure. To rightfully compare the dimensional parameters with the observational data we need to know some quantities like the disc scale length when it was axisymmetric several Gyrs before and the total disc mass. These characteristics are hard to obtain and they are subject to many errors. That leaves us with four dimensionless quantities: the opening angle of X-structures rays φ , the sharpness parameter r_X/s_X , the ellipticity of the isophotes ε_X and Sersic index n_X . Here we present the results only for two of them, φ and r_X/s_X . For n_X , we assume that it is equal to one in the present work. For ellipticity ε_X , we found that it mainly falls in the range between 0.2 – 0.5 for the considered galaxy models although there are some interesting exceptions when it takes negative values. It also shows some trends depending on the bar viewing angle and the setup of the photometric model. But, mostly due to lack of space and the desire to not overcomplicate the discussion, we prefer to not discuss it here.

4.1.1 Concept of “ideal” values of parameters

Since numerical models allow one to extract a bar by means of some dynamical considerations, we would like to exploit this possibility as much as possible to understand more accurately

² We note that the observational studies usually consider discs with breaks as in Kim et al. (2014) rather than AT discs. For further discussion, we assume that these two photometric models, although quite different, are used to describe the same physical situation at least in the context of SB galaxies, namely the change of density profile slope due to the bar.

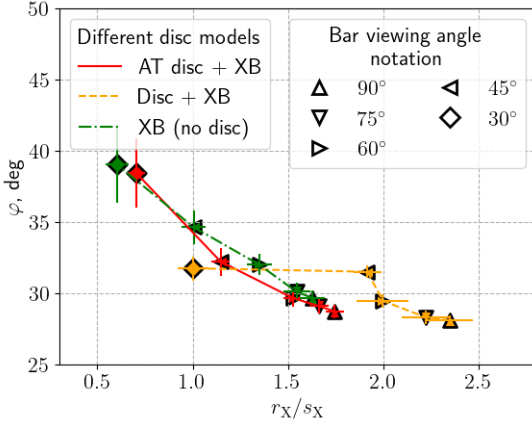


Figure 6. Impact of different photometric models of the disc and the bar viewing angle on the measured values of opening angle φ and the sharpness parameter r_X/s_X of the X-shaped bulge photometric model.

the impact of various non-physical effects. To this aim, we construct images depicting only bar particles like that shown in Fig. 1 for most of the images of the simulated galaxies that we decompose below. We use such images with only a bar component to compare the parameter values of the B/PS bulges obtained from the usual multi-component decomposition with the parameter values obtained if there were no disc screening the B/PS bulge. Essentially, analysis of the “pure” B/PS bulges allows one to obtain “ideal” values of parameters in a sense that parameters are then independent from the chosen disc model and the models of other photometric components. Comparison with “ideal” values of parameters allows us to understand more clearly how changes in the photometric model (for example, in disc model) affect the results of the decomposition.

4.1.2 Different photometric models of the disc

In photometric studies of the disc galaxies, it is customary to consider the photometric model of an exponential disc and its derivatives (broken exponential, truncated, anti-truncated discs). Here we investigate how the choice of the photometric model affects the parameters of B/PS bulge. We consider two types of disc models: a simple exponential disc and an AT exponential disc (see Section 3). Fig. 6 shows how the value of the opening angle φ and the sharpness parameter r_X/s_X depend on the bar azimuthal viewing angle for these two photometric models and for a pure B/PS bulge (see the previous subsection). The figure contains some important information that concerns the interpretation of observational data. First, if the bar is seen nearly side-on (azimuthal angle from 75° to 90°), we observe a B/PS bulge with a quite prominent X-structure (r_X/s_X from 1.5 to 2.5). In terms of opening angles, the choice of the disc model is rather insignificant in this case: the difference between AT disc model and a simple exponential disc model is about 1° . Both of these models give values of the opening angle that are smaller than “ideal” values (green curve) by about 2° , although they start to diverge for smaller bar rotation angles. Thus, different disc models produce nearly consistent values of the opening angle for the bar viewed side-on and the resulted values are close to “ideal” values in this case. However, in terms of another parameter - the sharpness parameter - the application of different disc models lead to quite distinct measured values. An application of a simple disc model leads to

larger values of this parameter, i.e. it leads to a more pronounced X-shape than it actually is.

When we rotate the bar for more than about 30° (up to 60°) the B/PS bulge shrinks to such a degree that the observed profile is substantially affected by choice of the disc model. Here we observe a large discrepancy not only for the sharpness parameters but for the opening angles too. A simple exponential disc model gives the values that are less than “ideal” ones by about 5° - 7° .

One more important thing we would like to note is that an AT disc model works a bit tricky for bars rotated less than 60° . For such bar orientations, the model tends to increase its density scale length of the hole h_T . In other words, the hole is gradually washed out as we rotate the bar. This happens because we observe the galaxies edge-on and observe the integrated luminosity profile. The problem is that the disc can have some additional asymmetric components like ansae (see Fig. 1). With the bar rotation, they also rotate, and at some point we stop to distinguish the intensity dip between them. In practise, we fix h_T value if the ratio R_T/h_T becomes greater than two. In this case, the model has a plateau in the centre instead of a hole. Nevertheless, Fig. 6 indicates that such a degenerated AT disc model is still better than a simple exponential disc model, especially if the X-shaped bulge model turns out to have a small value of the sharpness parameter.

4.1.3 Impact of disc inclination

Although our sample of real galaxies mostly contains galaxies seen edge-on we should confirm whether our results depend on small inclinations of the disc plane or not. A problem here is that the light coming from the inclined disc is mixed with that produced by a B/PS bulge, and the more inclined disc we take the more the disc model affects the bulge. To accurately analyse consequences of disc inclination, we considered four different cases. First, we check how the parameters of B/PS bulge itself change with an inclination if there were no disc. To this aim, we take a pure B/PS bulge extracted by means of the dynamical decomposition and constructed corresponding images for different values (from 2° to 6°) of the disc inclination angle. Then we fit our X-shaped bulge photometric model to each of the images. Fig. 7 (top left) shows the dependence of the opening angle φ and the sharpness parameter r_X/s_X on disc inclination and the bar azimuthal angle. The answer that follows from the figure is rather simple. A slightly inclined B/PS bulge is almost the same as not an inclined B/PS bulge. Both the opening angles and the sharpness parameters have almost the same values for inclined and not inclined B/PS bulges. This is an important result because the problem then has one less degree of freedom, which in principle could exist if the properties of the bulge strongly depended on inclination.

The next step is to consider how the presence of the inclined disc affects the parameters of B/PS bulges. At this step, we analyse the whole model consisting of all stellar component particles. We check the behaviour of three different photometric models of the disc: a) inclined AT disc (Fig. 13, top right) b) not inclined AT disc applied to actually inclined disc (Fig. 13, bottom left) c) not inclined simple exponential disc applied to inclined disc (Fig. 13, bottom right). The last two cases should also be considered, since the inclination of the disc, although it can be viewed as a free parameter, cannot be reliably estimated in some cases due to the actual resolution of the image and the presence of other photometric components. A general conclusion from the figures is that the disc inclination does change the values of the opening angles and the sharpness parameter. The best photometric disc

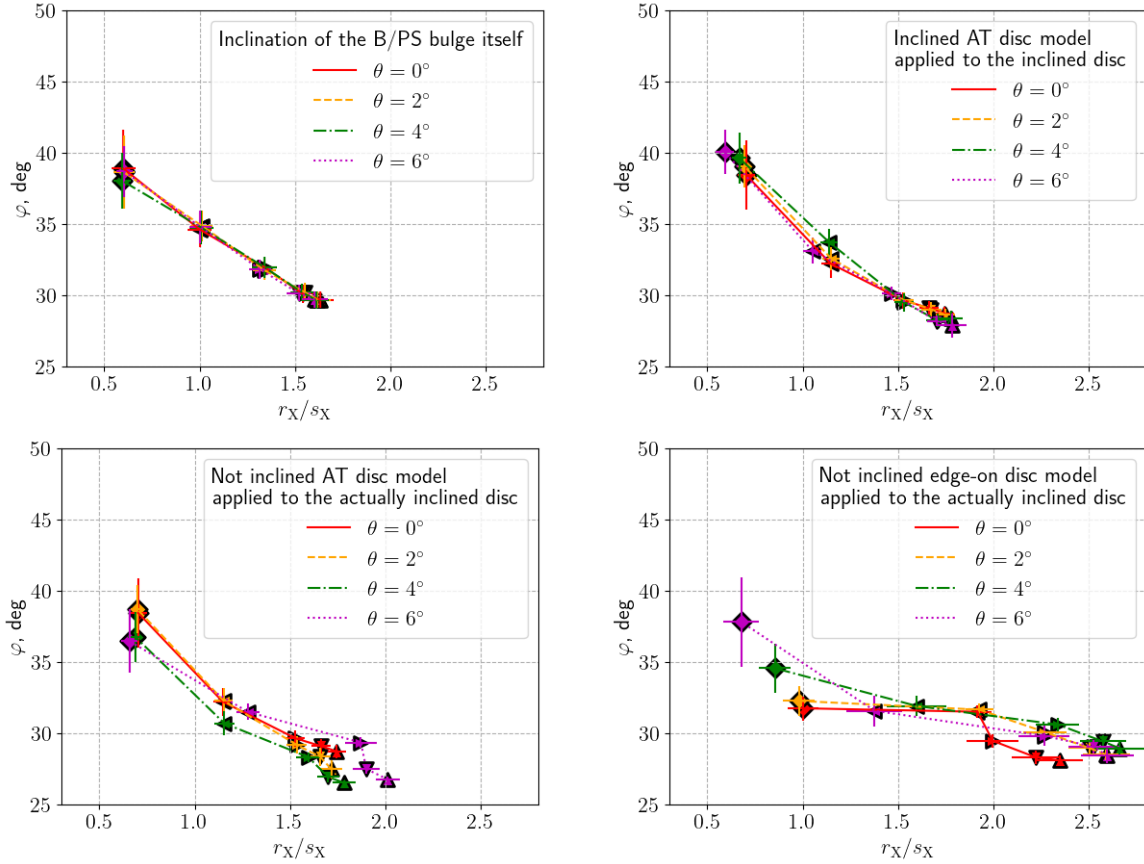


Figure 7. Impact of different photometric models of the disc and the bar viewing angle (symbolic notation follows that from Fig. 6) on the measured values of opening angle φ and the sharpness parameter r_X/s_X of the X-shaped bulge photometric model for different inclinations of the disc plane.

model that gives the values that are most consistent with the ideal ones is an AT inclined disc model. In this case, there is almost no distinction between the curves as in the case of the pure B/PS bulge. A photometric model of a not inclined AT disc but with the fixed inclination $i = 90^\circ$ applied to actually inclined disc results in the opening angles that differ from “ideal” values for about $2^\circ - 3^\circ$ depending on the bar orientation and disc inclination. The value of the sharpness parameter also slightly changes. As can be seen from the figure, an application of a simple disc model (without an inner truncation) leads to a poor estimation of B/PS bulge parameters especially in case of a bar major axis close to LoS. The situation repeats that for not inclined discs with no essential changes for the better or worse.

4.1.4 Other photometric components. Case of co-existing bulges

One of the possible problems of the photometric decomposition of disc galaxies is that the different types of bulges can co-exist in one galaxy. A well-known example is NGC 4565 where two types of bulges are distinguished, a boxy bulge and the so-called pseudobulge (see [Kormendy & Barentine \(2010\)](#)). The co-existence of different bulge types were also studied by [Erwin et al. \(2015\)](#) where authors distinguished discy and classical bulges. Most of real galaxies from our sample also seem to contain some central component which is not the part of the B/PS bulge. Therefore, we would like to check how the parameters of our B/PS bulge photometric model are affected by the presence of a bulge

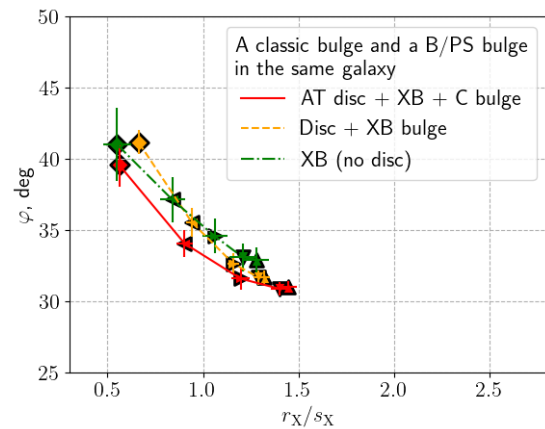


Figure 8. The dependence of the opening angle φ and the sharpness parameter r_X/s_X of X-shaped bulge model on the bar viewing angle (symbolic notation follows that from Fig. 6) for three different combinations of dynamical subsystems (see text for details) of the galaxy model with co-existing classical bulge and B/PS bulge. “C bulge” stands for a classical bulge.

of a different physical nature. To this aim, we use a galaxy model from [Smirnov & Sotnikova \(2018\)](#) that initially has a spherical Hernquist bulge on top of the axisymmetric exponential disc (see Tab. 1). This model has the same parameters as the “main” model except it has a classical bulge component with $M_b/M_d = 0.2$

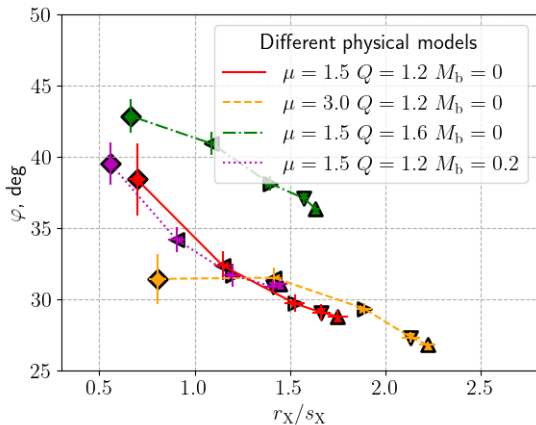


Figure 9. The dependence of the opening angle φ and the sharpness parameter r_X/s_X of X-shaped bulge model on the bar viewing angle (symbolic notation follows that from Fig. 6) for four different galaxy models from Tab. 1.

and $r_b = 0.2R_d$. We analysed it in the same way as the previous ones. First, we performed the dynamical decomposition and cut a B/PS bulge component based on the frequency analysis. Then we fit our X-shaped bulge photometric model to images with only a B/PS bulge to obtain “ideal” values of parameters (see section 4.1.1). Next, we consider two cases: the first, when the image is constructed only from disc and B/PS bulge particles, and the second, when the image includes all components, namely, a disc, a B/PS bulge, and a classical bulge. In the first case, we fit XB model along with AT disc and in a second one we fit a Sersic bulge photometric model along with XB and AT disc components. The former case should be considered because the resulted deviation from ideal values (if any) can arise due to the disc component. Fig. 8 show how the geometric parameters of B/PS bulge vary in all three cases depending on the bar orientation. As can be seen from the figure, the values of opening angles and the sharpness parameter are slightly different in each case. The presence of a classical bulge slightly lowers the opening angles although the difference is not that large, about 3° if the bar is rotated for about 45° and smaller for other bar orientations. In general, Fig. 8 shows that we indeed can hope to retrieve the values of B/PS bulge parameters close to real ones if several bulges co-exist in the same galaxy.

4.1.5 Impact of the physical parameters of the galaxies on the B/PS bulge parameters

Different physical models of galaxies give rise to quite different types of bars (for example, bars with a barlens or a peanut-shaped bars (Salo & Laurikainen 2017; Smirnov & Sotnikova 2018)). Naturally, the morphology of B/PS bulges that are extensions of the bars in the vertical direction also depends on the galaxy physical parameters. General trends in evolution of B/PS bulges and their X-structures in different disc models were thoroughly investigated by Smirnov & Sotnikova (2018). One of the important conclusions obtained by the authors was that the smallest opening angles should be observed in galaxies where dark matter has a significant contribution to the overall gravitational field within the optical radius of the disc, that is, in dark matter dominated galaxies. However, in Smirnov & Sotnikova (2018) the angles were measured based on the density distribution along the photometric cuts. First, we want to ensure that the same conclusion holds if we

use our new photometric model of the X-shaped bulge. There are also some other notable trends that were observed by Smirnov & Sotnikova (2018). For example, opening angles of the X-structure increase with an increase of the initial value of Toomre parameter Q in the disc or with an addition of a spherical bulge component to the model. We would like to verify these trends using our X-shaped bulge model. To this aim, we consider four representative models from Smirnov & Sotnikova (2018) (see Tab. 1 in the present work). For each of the models we select only one time moment again, namely $T \approx 6$ Gyrs after the beginning of the simulations for models with $\mu = 1.5^3$ and $T \approx 7$ for the model with $\mu = 3$. We consider a later time moment for the model with $\mu = 3$ since the bar in this model is formed about 1 Gyr later than in other models. We constructed images for each of the models for different bar orientations around disc axis and performed the photometric fitting in each case. All images were fitted by the combination of AT disc and B/PS bulge photometric models. The results are presented in Fig. 9. As can be seen from the figure, the model with the heaviest dark halo ($\mu = 3$) is indeed distinct. It shows the smallest opening angle of all models (in case of a side-on bar), although the difference between this model and our “main” model is not that large ($\approx 2^\circ$ for a side-on bar). At the same time, B/PS bulges in these models are quite different in terms of the sharpness parameter. In the model with the heavy halo, we observe a more prominent intensity dip between the rays (see Fig. 4 for reference). We should note that the transition of a bar azimuthal angle from 45° to 60° in this model seems rather unnatural as the opening angle value does not increase while the B/PS bulge substantially shrinks which is identified by a decrease in the sharpness parameter value. Such a behaviour seem to be caused by a complex structure of the B/PS bulge itself. As was shown by Parul et al. (2020) the appearance of the X-structure ray can be associated with the existence of some particular orbital family of quasi-periodic orbits. Thus, we can assume that the mix of equally populated orbital families can produce the density peaks in a rather wide strip. But the overall picture should also depend on the bar viewing angle since different families tend to occupy different regions of the bar (Portail et al. 2015; Parul et al. 2020). Therefore, if for a side-on bar we observe an imprint of only one orbital family there is a possibility that we start to distinguish some other families along with the first one in case of a rotated bar. A detailed orbital analysis of the model should clarify this issue.

A model with $Q = 1.6$ and a model with a classical bulge also show values of opening angles consisting with those obtained by Smirnov & Sotnikova (2018). The model with $Q = 1.6$ shows a rather large opening angles for all bar orientations in comparison the “main” model, from about 36° to 42° . The model with a classical bulge is close to the “main” model in terms of opening angles but show although not that distinct but still considerably smaller values of the sharpness parameter. In general, Fig. 9 demonstrates that the B/PS bulge parameters, as expected, depend both on the physical conditions in the disc and the structure of other physical components. But what is important here is that using our new photometric model we capture the different trends observed for different physical models like those obtained by Smirnov & Sotnikova (2018). It is also important that the sharpness parameter seems to be a good indicator of a bar azimuthal viewing angle. Although, we emphasise that we consider only four models here.

³ This is the same one we work with in the previous subsections considering our “main” model.

Therefore, this statement should be strictly verified on the larger sample of galaxy models.

4.1.6 Finishing remarks about numerical models

Concluding this subsection we would like to stress out that we do not pursue a goal to investigate as many possible physical models as we can or trends in their evolution here. No, our goal here was different. We wanted to ensure that the use of the X-shaped bulge photometric model leads to sensible results, that is:

- (i) for different geometric configurations arising due to the possible disc inclination and the rotation of the bar major axis around disc axis we can hope to retrieve “true” values of the X-shaped bulge parameters,
- (ii) that we can do it in case of a composite inner structure of the galaxy (although we considered here a relatively simple case),
- (iii) the application of the X-shaped model at least reproduces some qualitative results obtained by [Smirnov & Sotnikova \(2018\)](#).

In a way, this can be called a “debugging” of the X-shaped bulge model, that is, we apply various tests to see whether it works properly in different situations.

It is also important that we obtained some reference points such as the lower end of the opening angles range which is about 26° . This value is measured in the model with $\mu = 3$ for a side-on bar. In [Smirnov & Sotnikova \(2018\)](#) we showed that the X-structure in this model demonstrates the smallest opening angle of all thirteen models considered there. We expect that the B/PS bulges of real galaxies should rarely have X-structure angles smaller than this value, because to detect such a small value, one needs to detect a bar viewed side-on in a galaxy with a rather heavy dark halo, plus at later stages of its evolution. This is indeed possible, but should still be a relatively rare case.

5 REAL GALAXIES

5.1 Data

In order to apply our method to the images of real galaxies, we compiled a sample of galaxies by combining the sample of [Ciambur & Graham \(2016\)](#) with the sample of [Savchenko et al. \(2017\)](#), that gave us in total 31 galaxies with prominent B/PS bulges. Table 2 shows the general parameters of the sample galaxies compiled from HyperLEDA ([Makarov et al. 2014](#)) and NASA/IPAC Extragalactic Database (NED)⁴ databases. In this section we describe the data preparation for these galaxies.

Optical images were retrieved from the Sloan Digital Sky Survey DR12 database⁵ ([Eisenstein et al. 2011](#)) in r-band. The following data preparation pipeline was identical to the one from [Savchenko et al. \(2017\)](#) and included following steps for every image:

- (i) adjacent SDSS fields were combined into single image using SWARP package ([Bertin et al. 2002](#));
- (ii) background flux was approximated using 2D polynomial of objects free regions of the image and subtracted;

- (iii) the position angle of the galaxy was estimated using method from [Martín-Navarro et al. \(2012\)](#) and the image was rotated such that the galaxy was oriented along the x-axis of the image;

- (iv) a point spread function of the image was constructed using a set of isolated non-saturated stars on the image;

- (v) all the objects on the image except for the galaxy were masked out using object catalogues made by SEXTRACTOR package ([Bertin & Arnouts 1996](#)) to exclude them from the analysis.

- (vi) Sigma images were automatically generated using IMFIT software based on the gain, read noise, and intensity of the original subtracted sky background values which all can be found in SDSS database for the corresponding fields. The precise equation is the following:

$$\sigma_i^2 = (I_{d,i} + I_{\text{sky}})/g_{\text{eff}} + N_c \sigma_{\text{rdn}}^2 / g_{\text{eff}}, \quad (13)$$

where $I_{d,i}$ is the data intensity, I_{sky} is the intensity of the original subtracted sky background, σ_{rdn} is the read noise value, N_c is the number of separate images combined to form the data image, and g_{eff} is the “effective” gain (the product of the gain and N_c).

The IRAC $3.6\mu\text{m}$ images were downloaded from the Spitzer Survey of Stellar Structure in Galaxies database⁶ (S4G, [Sheth et al. \(2010\)](#)). These images were also corrected for the background and rotated identically to the optical ones. Objects masks and sigma-images were adopted from [Salo et al. \(2015\)](#), and we used instrumental PSF from the mission website⁷. For all SDSS and IRAC images the individual pixel weights w_i were calculated as a reverse square of the corresponding sigma values, $w_i = 1/\sigma_i^2$.

5.2 Results

Although we assume that B/PS bulges of the modelled galaxies should resemble the bulges of real galaxies, the physics of real galaxies is definitely richer. In particular, the influence of a gaseous component, star formation, supernova feedback, not to mention our doubts as to whether we model the physics of dark matter correctly, are the main factors that we miss in our models. Although these factors are not directly associated with B/PS bulges they determine the properties of the bar (its pattern speed and size) thus indirectly affecting the B/PS bulges too. We also do not possess knowledge of initial conditions in the disc when it began to form the bar. All these problems are fairly well-known problems of numerical modelling which are currently addressed in many numerical studies. Therefore, if some deduced photometric model works fairly well in the case of modelled galaxies it does not necessarily adequately represent B/PS bulges in real galaxies. To clarify this, we start this section with a few important examples showing how the X-shaped bulge model works in the case of real galaxies.

5.2.1 NGC 128

We start with one of the most prominent candidates among the galaxies with a B/PS bulge and X-structures, NGC 128. This galaxy is a famous galaxy where the first X-structure was distinguished ([Burbidge & Burbidge 1959](#)). Together with NGC 126 (E/SB0),

⁴ <http://ned.ipac.caltech.edu/>

⁵ <https://www.sdss.org/dr12/>

⁶ <http://irsa.ipac.caltech.edu/data/SPITZER/S4G/>

⁷ <https://irsa.ipac.caltech.edu/data/SPITZER/docs/irac/calibrationfiles/psfprf/>

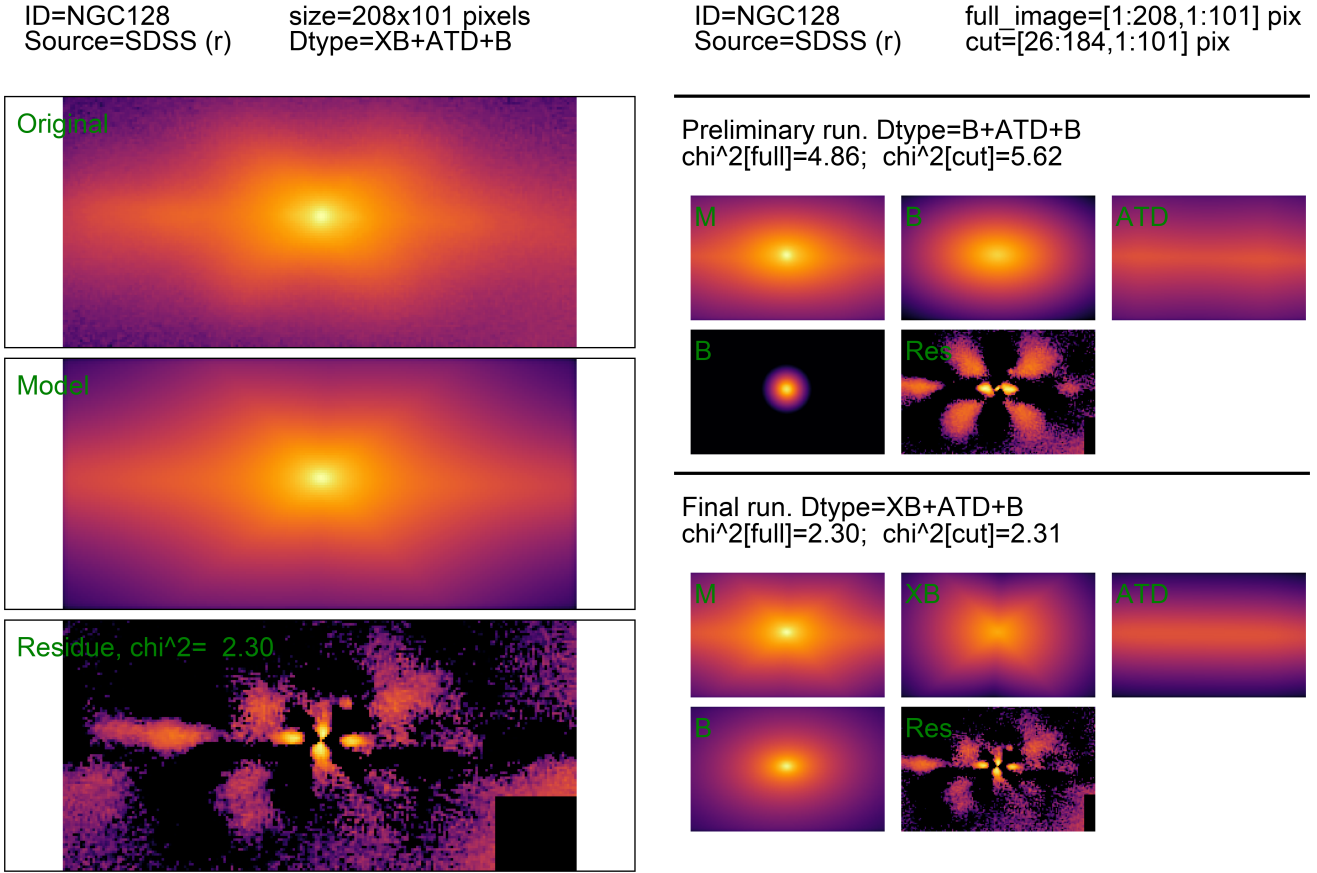


Figure 10. The photometric decomposition of NGC 128. *Left:* the original galaxy image (*top*), the best-fit photometric model (*middle*) and the residue image (*bottom*). *Right:* the images of the individual photometric components and the residue image for the preliminary run with a simple Sersic bulge (*top*) and for the run with the X-shaped bulge model given by Eq. (5) (*bottom*). The auxiliary text above the images gives various details of the decomposition. We note that the images in the right column show the rectangle of a smaller area than full images from the left column (see auxiliary text). This smaller area roughly corresponds to the area where the most part of the B/PS bulge resides. We give two chi-square values, one of which is calculated over all pixels used for the decomposition (“chi²[full]”) and the second one which is calculated over the pixels only from this smaller area (“chi²[cut]”). The latter is more sensitive to the B/PS bulge model and is more convenient to use if we want to compare different models of the B/PS bulge.

NGC 127 (Sa), and NGC 130 (E5) and possibly NGC 125 (S0 pec) (Zwicky et al. 1965; D’Onofrio et al. 1999), this galaxy forms a group of galaxies (Peterson 1979). The outer disc region of NGC 128 is substantially disturbed by the gravitational interaction with NGC 127, which causes the appearance of a bridge connecting one to another (Burbidge & Burbidge 1959). The analysis of the gas kinematics showed that the central area (~5 arcsec, roughly one-quarter of the peanut projected size) harbours the counter-rotating gaseous component (D’Onofrio et al. 1999). Nearly on the same space scale (about one fifth of the larger peanut size) Ciambur & Graham (2016) identified the so-called “nested peanut” residing in the larger one. Needless to say, this galaxy is not an easy target for the 2D photometric decomposition. Mostly due to its peculiar inner structure.

The decomposition procedure follows our usual pattern. It consists of two stages, namely a preliminary stage at which we find the initial conditions for the X-shaped bulge fitting the B/PS bulge by a Sersic function and the final stage where we start from previously obtained set of parameters to find the best-fit model. We found by trial and error that there is a problem with the before-mentioned inner component boiling down to the fact that

it should be somehow represented in the initial photometric model. Otherwise, the outer X-shaped bulge tends to degenerate into the inner bulge. Therefore, our initial photometric model consists of AT disc and two bulges, one of which has a fixed Sersic index $n = 1$. The second one has free parameters except for the PA which is fixed in order to prevent the bulge degeneration into two lobes of the B/PS bulge at the preliminary run (we free this parameter at a final run). The results of our decomposition procedure (best-fit model and residue images), as well as individual images of all components for two runs are shown in Fig. 10. We exclude the outer part of the disc from fitting because of the disturbance caused by the gravitational interaction with NGC 127, and fit only the smaller area that nevertheless contains the whole peanut and small ansae that can indicate where the disc inner truncation should start. Chi-square values (see the caption for the individual components images) indicate that the modification of the Sersic bulge to the X-shaped bulge leads to a significant improvement of the residue. Four lobes appearing in the preliminary run residue image are mostly dispersed to the final run and the central peculiar component becomes the main source of errors. We also note that the second bulge representing an inner component becomes close

Name	T	M_r mag	d_{25} arcmin
PGC002865	5.8	-20.01	1.78
PGC010019	3.0	-20.96	0.78
PGC021357	3.3	-20.65	1.14
PGC024926	2.0	-19.36	1.70
PGC026482	3.1	-20.66	1.17
PGC028788	0.5	-20.35	0.85
PGC028900	0.9	-21.55	1.00
PGC030221	3.0	-20.44	1.12
PGC032668	0.0	-20.59	1.04
PGC034913	3.0	-20.89	1.91
PGC037949	1.4	-20.82	1.32
PGC039251	-0.9	-20.73	1.69
PGC044422	0.4	-21.13	0.72*
PGC045214	1.0	-21.41	0.89
PGC053812	3.9	-21.51	1.10
PGC055959	2.0	-21.38	1.02
PGC069401	1.0	-21.97	1.10
PGC069739	5.2	-20.92	2.00
ASK361026.0	4.6	-21.77	0.44*
ESO443-042	3.0	-20.90	2.81
NGC128	-2.0	-22.30	3.16
NGC678	3.0	-20.98	3.09
NGC2549	-2.0	-20.07	3.63
NGC2654	2.0	-19.69	4.47
NGC2683	3.0	-19.82	9.55
NGC3628	3.1	-19.49	10.96
NGC4111	-1.3	-19.68	1.78
NGC4469	0.3	-19.07	2.88
NGC4710	-0.9	-20.53	4.37
NGC5529	5.1	-20.71	5.75
NGC7332	-1.9	-19.33	2.95

Table 2. Parameters of the sample galaxies: name, T-type, absolute magnitude in r-band and the apparent diameter.

to the X-shaped bulge in terms of their linear scales ($r_X/r_B \approx 1.2$). Although this issue is not that severe if we consider their respective Sersic indexes which are quite different ($n_X = 1$ versus $n = 2.6$).

We performed an additional run with a fixed to zero ellipticity of the inner component to see whether we can somehow lessen the degeneracy. In other words, we try to fit a bulge component with completely circular isophotes. Thus, we assume that the inner component is rather not a nested peanut but more like a small pseudobulge arising due to gas concentration in the central area of the galaxy. Due to lack of space, we do not provide the corresponding figure here, but it is available in online materials (see NGC 128* there). We found that for such a restricted model of an inner component the X-shaped bulge and the Sersic bulge representing the inner component turn out to have quite distinct sizes ($r_X/r_b \approx 6$), which implies a lesser degree of degeneracy. However, the residue worsens and the corresponding chi-square value increases from 2.3 to 3.0. Although, it is still better than a chi-square value of a preliminary run, $\chi^2 = 5.62$.

It should be stressed out that in both types of the decomposition (with the fixed and free ellipticity) the resulted values of opening angles and linear scales of the X-shaped bulges are close to each other ($\varphi = 44^\circ$ in both cases and $r_X \approx 3.0$ kpc for the free run and $r_X \approx 2.7$ kpc for the run with the fixed ellipticity). There are indeed some notable changes in the value of the second length scale s_X of the X-shaped bulge, $s_X \approx 2.7$ kpc versus $s_X \approx 4$ kpc, respectively, and according to that the sharpness

parameters have quite different values too ($r_X/s_X \approx 1.11$ versus $r_X/s_X \approx 0.67$). In other words, what changes between these two runs is the sharpness of the observed X-structure. In a sense, this behaviour resembles the behaviour of different disc models applied to the same numerical model which we investigated in Section 4. In that case, there were also changes in the sharpness parameter while the opening angles turn out to be close to each other.

We should also note some important things concerning the nature of the inner component (nested peanut?). The residue image of a typical peanut usually shows four pronounced lobes (see Fig. 10, preliminary run) if we fit the B/PS bulge by a Sersic function. If we assume that the inner component is a nested peanut similar to the outer one, then it is reasonable to further assume that the residue image should show four inner lobes in this case. There are indeed four lobes seen in the residue image (Fig. 10, final run), but two of them appear in the disc plane and the other two sit on the line perpendicular to the disc plane. Therefore, the residue of the inner structure does not resemble the residue of the outer structure. Although there may still be some doubt, since the residue of the central area was obtained by subtracting the B/PS bulge and disc photometric models, we believe that the structure of the residue indirectly indicates that the inner component is at least not an ordinary peanut. In principle, such a structure of the residue can appear due to the presence of the inner (second) small bar if its major axis is oriented close LoS and the disc plane is slightly inclined. Based only on the residue structure we also cannot rule out the possibility that there is simply a small flattened bulge (either classical or pseudo-bulge formed via gas inflow and subsequent star formation). We are not going to pursue further this question here and leave it for future studies.

5.2.2 ESO 443-042

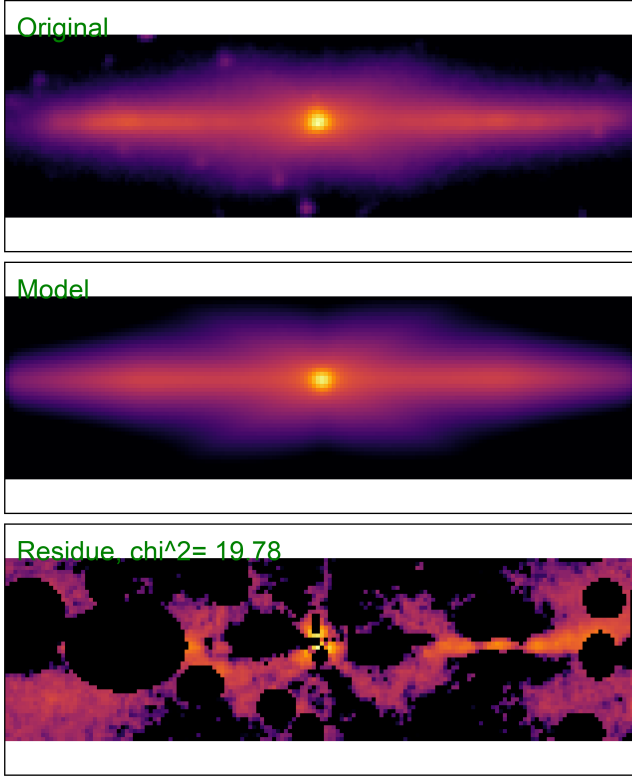
This is a peculiar galaxy where Ciambur & Graham (2016) identified a peanut with a very small ratio of vertical to in-plane extent, $z_{\Pi, \max}/R_{\Pi, \max} \approx 0.26$ (in notations of Ciambur & Graham (2016)) which translates into the angular measure to obtain $\psi = \arctan(z_{\Pi, \max}/R_{\Pi, \max}) \approx 14^\circ$. At the same time, Laurikainen & Salo (2017) identified quite a typical B/PS bulge with sizes ratio about $a_X/b_X \approx 0.8$ which corresponds to an angle value $\varphi \approx 39^\circ$. We note that Ciambur & Graham (2016) used a $4.5\mu\text{m}$ image, while Laurikainen & Salo (2017) used $3.6\mu\text{m}$ data. We also use $3.6\mu\text{m}$ data.

The results of our decomposition for ESO 443-042 is shown in Fig. 11. We masked a bright feature seen at the left side of the disc (seen as a dark blob at the residue image). It has no symmetrical partner at the other side of the disc plus it significantly affects the disc component if included. Again, we should deal with two types of bulges at the preliminary stage. Compared to NGC 128 case, these two bulges are quite distinct in terms of their linear sizes ($r_X/r_B \approx 23$). Therefore, there is no problem with the possible degeneracy of the components.

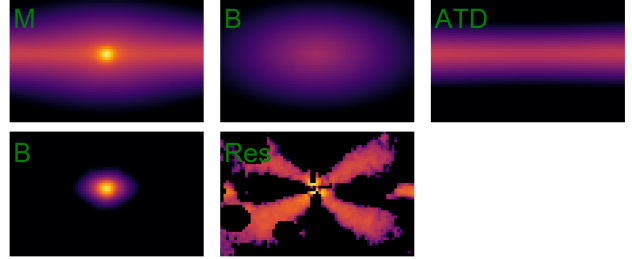
Concerning the X-shaped bulge in this model, we note the following. One can see four rather bright lobes in the preliminary run residue image. After we transform a Sersic profile into the X-shaped bulge model, these lobes mostly disperse (although not completely). Chi-square value is substantially reduced too (about one and a half times). However, it is still rather large ($\chi^2 \approx 21$). Does it mean that our photometric model is no good? From a strict point of view, yes, it does. However, we should point out that for many galaxies from S4G catalogue encountering such a large value of chi-square in 2D decomposition is not that unusual

ID=ESO443-042 size=158x46 pixels
Source=S4G (3.6mm) Dtype=XB+ATD+B

ID=ESO443-042 full_image=[1:158,1:46] pix
Source=S4G (3.6mm) cut=[43:115,1:46] pix



Preliminary run. Dtype=B+ATD+B
chi²[full]=28.48; chi²[cut]=31.11



Final run. Dtype=XB+ATD+B
chi²[full]=19.78; chi²[cut]=21.10

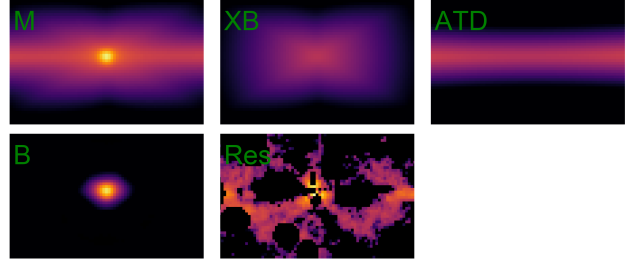


Figure 11. The photometric decomposition of ESO 443-042 galaxy (see caption of Fig. 10 for details).

(see Salo et al. 2015). In principle, the addition of other photometric components can help, but in this particular case, we believe that it is unnecessary. The residue image shows that there are three main sources of errors, namely a central component, right bright blob (although almost masked), and the residue from the X-shaped bulge. The central component mostly occupies the region with a spatial scale close to that of the second bulge and therefore should not strongly affect the X-shaped bulge geometric parameters. The blob clearly lies outside the X-shape bulge area and for this reason also should not significantly affect the X-shaped bulge model (although its presence indeed changes the disc model and therefore indirectly affect X-shaped bulge model but its influence should be dumped by the disc inner truncation).

The geometric parameters of the X-shaped bulge of this galaxy are rather typical. An opening angle φ has a value of about 30° and the sharpness parameter value is about 1.3. The obtained opening angle value is not consistent with that obtained neither by Laurikainen & Salo (2016), nor by Ciambur & Graham (2016). We see no apparent reason for B/PS bulge identification to produce a very flattened bulge as in Ciambur & Graham (2016). Perhaps, strong inhomogeneities in the disc that we masked could contribute to this matter. As for Laurikainen & Salo (2017), their unsharp-masked image shows two large lobes instead of four separate rays coming from the disc centre (in contrast to our residue image of the preliminary run shown in Fig. 11). We discuss this matter more thoroughly in Section 6.

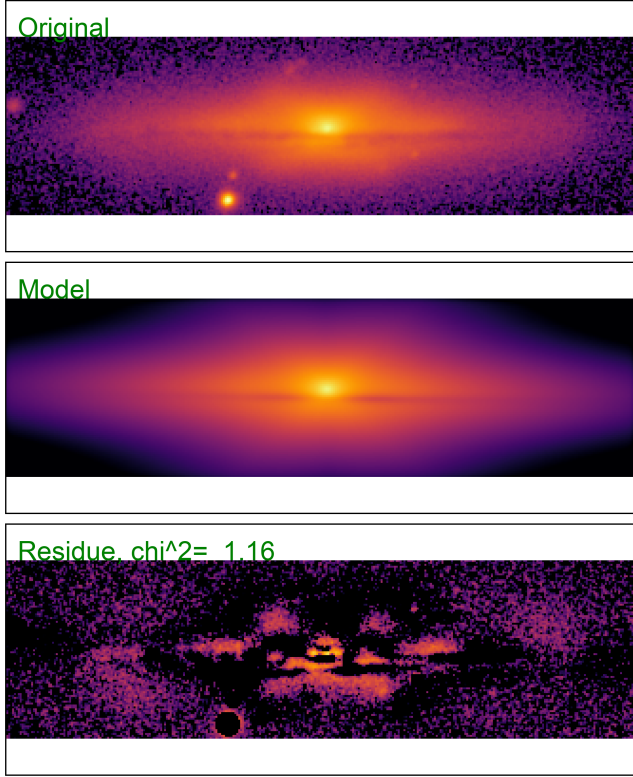
5.2.3 PGC 24926

The next galaxy which we would like to discuss in more detail is PGC 24926. This galaxy is intersected by an almost straight dust line visibly shifted from the disc plane. We show this example to demonstrate how the X-shaped bulge model works in case of a galaxy having a dust feature. Fig. 12 shows the result of the decomposition. We can see that the X-shaped profile in residue images becomes less pronounced from the preliminary to the final run. Although the improvement is not as noticeable as in previous cases. We note that the second bulge shrinks after modification of the photometric model, while the dust disc becomes thinner. The resulted peanut has a rather large opening angle $\varphi \approx 42^\circ$ accompanied by a small value of the sharpness parameter $r_X/s_X \approx 0.33$. We also note that the centre of the dust disc model turned out to be slightly shifted from the centre of the stellar disc. This effect is probably due to the slight inclination of the stellar disc plane to LoS.

5.2.4 Full galaxy sample

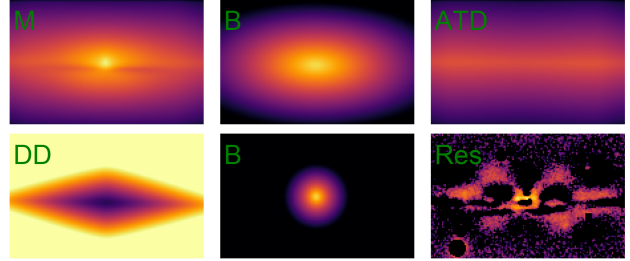
In Tab. 3 we present the values of X-shaped bulges geometric parameters for our galaxy sample. Due to lack of space, we cannot present the decomposition images for all galaxies here. Instead, we made them available at <https://vo.astro.spbu.ru/node/130> and refer an interested reader to look at them online.

ID=PGC024926 size=331x94 pixels
Source=SDSS (r) Dtype=XB+ATD+DD+B



ID=PGC024926 full_image=[1:331,1:94] pix
Source=SDSS (r) cut=[96:242,1:94] pix

Preliminary run. Dtype=B+ATD+DD+B
 $\chi^2[\text{full}] = 1.45$; $\chi^2[\text{cut}] = 2.53$



Final run. Dtype=XB+ATD+DD+B
 $\chi^2[\text{full}] = 1.16$; $\chi^2[\text{cut}] = 1.89$

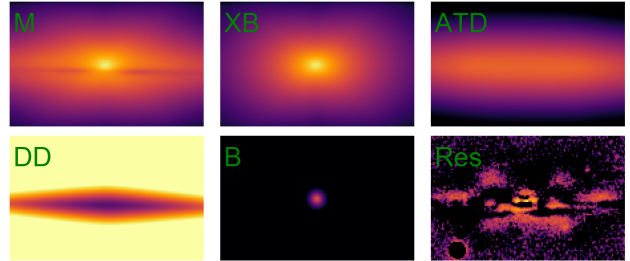


Figure 12. The photometric decomposition of PGC 24926 galaxy (see caption of Fig. 10 for details)

There are several general things we should mention concerning the full galaxy sample. First of all, the X-shaped bulge model works, that is, we indeed could find the reasonable photometric model for almost all galaxies from our sample (with some exceptions mentioned below). But the degree of the residue improvement due to a modification of a simple Sersic model to the X-shaped bulge model varies for different galaxies (see NGC 7332 in online materials for a “bad” example). There are also a few cases when we add some other components like a ring or a small central component after the preliminary run. The reason for this is that the ring (or Gaussian) tended to become part of the X-structure if it was included in the preliminary run. It is hard to say whether chi-square improves mainly due to changes in the bulge model or due to the addition of the new component in these cases (see PGC 10019 in online materials). Concerning the disc component, we represented it by an anti-truncated disc model (see Section 3) in all our galaxies. There are several cases when the hole degenerated and the disc showed a plateau instead of an intensity dip. We observed similar behaviour in numerical models in case of a bar having close to end-on orientation. Therefore, it is not surprising that for some real galaxies we observe a similar situation. The matter of disc inner truncations is interesting by itself, but it is beyond the scope of the present work and we will not discuss it further.

There are several galaxies from Savchenko et al. (2017) and Ciambur & Graham (2016) which we discarded after the preliminary analysis. These are PGC 21357, NGC 678, NGC 2549,

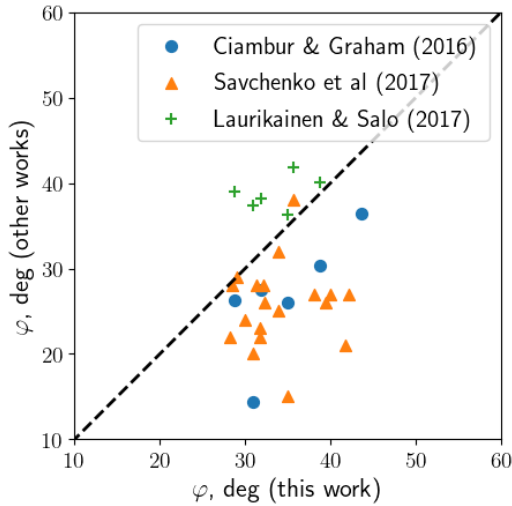
NGC 3628, NGC 4111, and NGC 4469. PGC 21357 is a galaxy with a very strong dust feature. The resulted photometric model which we obtained has an unreasonably small value of the sharpness parameter ($r_X/s_X \approx 0.3$), with an uncertainty compared with the value itself. This is due to the strong dust feature screening most of the central part of the X-shaped bulge. NGC 3628 has indeed a very nice B/PS bulge, but the dust has a very inhomogeneous structure that prevents the reliable disc parameters estimation. The same story goes for NGC 4469. NGC 678, NGC 2549, NGC 4111 mostly lack an X-shaped feature in corresponding residue images already at the preliminary stage. Therefore, an X-shaped bulge model tends to become a part of the disc or just the usual bulge (an X-shaped bulge with $r_X/s_X \approx 0$). Probably, we observe a bar nearly end-on in these galaxies which explains why they demonstrate boxy-like shape with no apparent X-shape feature.

6 COMPARISON WITH PREVIOUS WORKS

Fig. 13 shows how the opening values obtained in this work correlate with the values obtained by Ciambur & Graham (2016), Laurikainen & Salo (2017) and Savchenko et al. (2017) for the same galaxies. The overall picture seems rather unsatisfactory. In an ideal case, if the values do not depend on the method used, we should obtain strictly equal values. However, this is not true

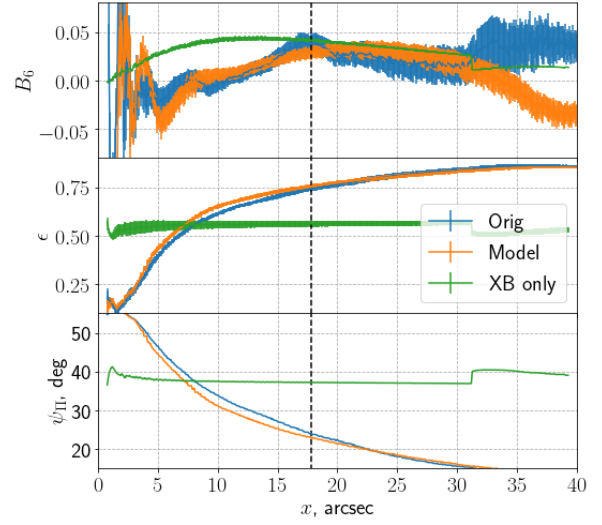
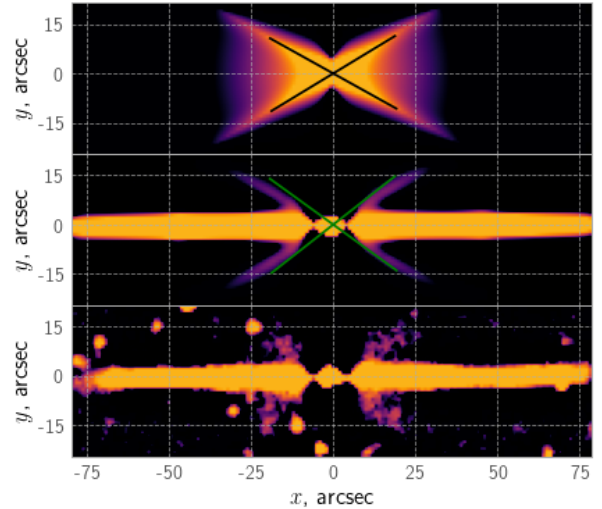
Table 3. Geometric parameters of X-shaped bulges for full galaxy sample.

Galaxy	r_X (kpc)	φ (deg)	r_X/s_X	ϵ_X
PGC002865	1.38±0.05	33.86±0.44	1.75±0.08	-1.00
PGC010019	2.55±0.04	29.96±0.50	1.51±0.07	-0.71±0.04
PGC024926	1.15±0.01	41.75±0.38	0.33±0.01	0.40±0.00
PGC026482	1.31±0.03	28.45±0.59	1.15±0.08	-0.67±0.06
PGC028788	1.64±0.04	39.47±0.82	0.85±0.09	0.41±0.03
PGC028900	2.47±0.06	31.76±0.37	1.82±0.06	-1.00
PGC030221	1.80±0.08	30.85±1.19	1.31±0.38	-0.48±0.44
PGC032668	1.52±0.05	29.01±0.32	1.45±0.13	-0.61±0.11
PGC034913	1.71±0.02	38.14±1.04	0.46±0.03	0.06±0.04
PGC037949	4.53±0.06	31.34±0.58	0.62±0.03	0.37±0.02
PGC039251	1.97±0.04	35.02±0.26	1.47±0.06	-0.86±0.02
PGC044422	1.85±0.03	31.67±0.32	1.62±0.04	-0.98±0.03
PGC045214	2.40±0.03	32.18±0.29	1.65±0.05	-0.89±0.04
PGC053812	2.96±0.12	32.33±0.40	1.30±0.23	-0.35±0.27
PGC055959	1.57±0.09	33.85±0.53	1.39±0.11	-0.95±0.04
PGC069401	2.84±0.03	42.11±0.73	0.79±0.02	0.29±0.02
PGC069739	2.14±0.05	39.96±1.85	0.46±0.04	0.25±0.03
ASK361026.0	2.24±0.02	28.27±0.22	1.71±0.03	-1.00
ESO443-042	3.77±0.21	30.92±1.48	1.28±0.15	-0.03±0.18
NGC128	2.94±0.03	43.59±0.36	1.11±0.02	0.20±0.01
NGC128*	2.65±0.02	44.24±0.31	0.67±0.01	0.30±0.00
NGC2654	1.52±0.01	34.98±0.51	0.58±0.02	0.35±0.01
NGC2683	1.18±0.01	31.89±0.17	0.90±0.03	-0.40±0.03
NGC4710	1.23±0.02	28.73±0.42	1.12±0.04	-0.15±0.05
NGC5529	2.68±0.08	35.59±0.91	1.97±0.15	-0.30±0.14
NGC7332	0.70±0.01	38.77±0.66	0.43±0.03	0.50±0.01


Figure 13. Comparison of the opening angle values obtained in the previous works and in this work for the same galaxies. For each of the works, with the results of which we try to compare our results, we intersected our galaxy sample with the galaxy samples considered in the mentioned works. The displayed points thus correspond to galaxies from three different sub-samples (which also partially overlap between each other).

for most of the considered galaxies. Rather, they try to avoid the line of equal values. There are also some trends that we observe in the figure. The opening angles from Laurikainen & Salo (2017) are larger on average than those we measure. The opposite situation is with Ciambur & Graham (2016) and Savchenko et al. (2017). Their values are smaller than ours on average.

Although it is not that rare that different methods produce


Figure 14. Comparison of the isophotes parameters of the original image, the total photometric model for this galaxy obtained in this work, and only the X-shaped bulge component for ESO 443-042 galaxy. *Top*: the dimensionless B_6 amplitude profile; *Middle*: the ellipticity of the isophotes ϵ ; *Bottom*: the polar angle of the peanut calculated as in Ciambur & Graham (2016). Dashed line marks the location of B_6 maximum in the original image.

Figure 15. Usharp-masked images of the X-shaped bulge component for ESO 443-042 galaxy (*top*), the total photometric model (*middle*), and original galaxy image (*bottom*) obtained using the same filter parameters and the intensity scales. The black cross highlights the location of the X-structure rays. The green cross (*middle panel*) highlights the location of the X-structure rays if they had an opening angle about 37° , which is the value measured by Laurikainen & Salo (2017) for this galaxy.

different results for the same galaxies, we would like to get a general idea of why this happens and happens in the manner shown in Fig. 13. To answer this question, we analyse in more detail how different measuring techniques work on the example of already discussed ESO 443-042 galaxy.

To compare our results with the results of Ciambur & Graham (2016) we apply the isophotal analysis similar to that used by Ciambur & Graham (2016) to the original galaxy image and the

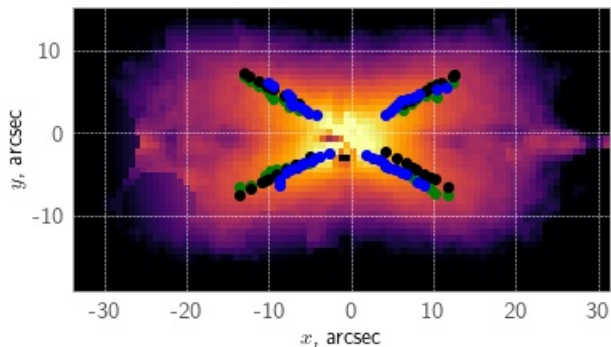


Figure 16. Comparison of approaches to measure X-structure opening angles in the present work and in [Savchenko et al. \(2017\)](#) for ESO 443-042. Green and blue dots correspond to the location of the density peaks identified along the elliptical cuts with ellipticities $\epsilon = 0.4$ and $\epsilon = 0.6$, respectively. Black dots mark the actual location of the X-structure rays in the X-shaped bulge model for this galaxy.

images of the total photometric model obtained in this work, and only the X-shaped bulge component extracted by 2D photometric decomposition. In Fig. 14 we plot the main parameters of the isophotes that [Ciambur & Graham \(2016\)](#) used to obtain the peanut angle. These are B_6 harmonic amplitude and the ellipticity of the isophotes ϵ . The peanut angle is calculated as follows:

$$\psi_{\text{II}} = -\arctan [(\epsilon_{\text{max}} - 1) \tan(2\pi/6)], \quad (14)$$

where ϵ_{max} is the ellipticity of the isophote that has a maximum B_6 value⁸. As can be seen from Fig. 14, B_6 profiles and the ellipticity profiles are close for the original image and for the total photometric model. However, when we apply isophotal analysis only to the X-shaped bulge component, we obtain drastically different results. Here observe a constant value of the isophotes ellipticity, and, moreover, it is considerably greater than that of the original image or the best-fit photometric model in the inner area and far smaller than those in the outer area. At B_6 maximum location ϵ has the value of about 0.56 for the X-shaped bulge component, while in the original image it is about 0.77. According to that, the peanut angle values are also quite different. In the former case, we obtain the value of about 38° , while in the second case the angle value is about 21° . Clearly, the only culprit responsible for the observed difference is a disc component. In fact, Fig. 14 directly indicates that the peanut angle value obtained based on B_6 harmonic is highly dependent on the disc contribution. With the addition of a disc to the B/PS bulge, the isophotes become more elongated, the ellipticity decreases and, according to Eq. (14), the angle value decreases too. We assume that the observed systematic shift of [Ciambur & Graham \(2016\)](#)'s angles to lower values for other galaxies can also be explained in a similar way.

Concerning the comparison with [Laurikainen & Salo \(2017\)](#)'s results, we should state that the strict comparison is hardly possible as the unsharp-masking procedure has some parameters that determine the outcome of the procedure. These parameters usually

⁸ We note that the equation we give here is different from that used by [Ciambur & Graham \(2016\)](#) for ψ_{II} evaluation. We assume that there is probably a typo in their equation, because ψ_{II} they indicated in their figure 1 is not the eccentric anomaly angle, but the polar angle. The eccentric anomaly for the peanut should be $2\pi/6$, while the polar angle should indeed depend on the isophotes ellipticity.

depend on the particular galaxy, are chosen by the observer and not specified. To understand more clearly how the unsharp-masking technique works for the B/PS bulge and their X-structures, we prepared the unsharp-masked images of the X-shaped bulge model, the total photometric model, and the original ESO 443-042 image using the same filter parameters and the intensity scales in both cases (Fig. 15). As can be seen from the figure, for the X-shaped model we find that unsharp-masking indeed highlights the locations of the X-structure rays (and quite accurately on top of it). However, in the case of a full galaxy image, the unsharp-masking transforms the whole bulge into two ear-like structures with the large intensity dip between them. The X-structures are less noticeable on the original image (the two left rays in particular), although they still can be identified. The next question is how we measure the parameters of these lobes. As far as we understand, [Laurikainen & Salo \(2017\)](#) measured them by hand, and this can introduce some errors, which result in the systematic shift of the opening angles. We also note that while experimenting with unsharp masking, we found that increasing the gradient contribution as much as possible, but to such a degree that the density peaks are still visible, helps to more accurately identify the X structure.

For completeness, we compare our approach with the approach used by [Savchenko et al. \(2017\)](#) on the example of ESO 443-042 galaxy although [Savchenko et al. \(2017\)](#) did not consider this galaxy in their sample. This can be done if we analyse the density distribution along the photometric cuts as it was done in [Savchenko et al. \(2017\)](#). One of the interesting aspects of that study was that the authors considered cuts not of the B/PS bulge model itself but of the image obtained by subtracting all components from the original image, except the one responsible for the B/PS bulge. We prepared such type of an image for ESO 443-042 (Fig. 16) and analysed the density distributions along the ellipses with different major axes values in a range from about 8 to 18 arcsec. We consider two sets of ellipses one with the ellipses ellipticity $\epsilon = 0.4$ (green dots) and the other one with $\epsilon = 0.6$ (blue dots). Along each of the ellipses, we identified four density peaks that correspond to the points where the rays of the X-structure intersect with the ellipses. For reference, we also added the set of points that highlight the location of the ray in our X-shaped bulge model for this galaxy (black dots). As can be seen, the location of all density peaks coincide remarkably well for all rays except the bottom right one but the difference there is not that large. The consistency that we observe directly indicates that the photometric cuts approach should produce results close to ours if other things are the same. According to that, there should be another reason for the systematic shift that we observe in Fig. 13. In Section 4, where we studied the impact of different disc models on the X-shaped bulge model, we showed that the application of a simple exponential disc model (without an inner truncation) lead to lower values of the opening angles with the effect stronger for close to end-on bars (see Fig. 6). [Savchenko et al. \(2017\)](#) indeed used an exponential disc model while we use AT disc model. Consequently, it is logical to associate the observed systematic shift with different disc models applied.

7 COMPARISON WITH THE MODELLED GALAXIES

Here we compare the modelled and real galaxies in terms of their X-shaped bulge parameters. Fig. 17 shows the data obtained for real galaxies superimposed on the data obtained for the modelled galaxies from Fig. 9. We can see that the real galaxies mostly

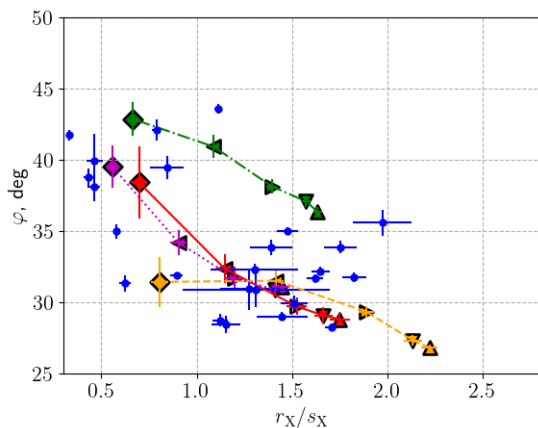


Figure 17. Comparison of opening angles and the sharpness parameters of the X-shaped bulges of real (blue dots) and simulated (triangles and hexagons) galaxies from Fig. 9.

follow the modelled ones in terms of their B/PS bulges. In terms of opening angles real X-structures span the range from about 27° to 44° . We note that the lower boundary value 27° translates into the aspect ratio about 0.51 which agrees quite well with the lower boundary found by Laurikainen & Salo (2017) for both real galaxies and N -body models they used (see their figure 8). We can also note that for the most of real B/PS bulges the sharpness parameter lies in the range from $r_X/s_X \approx 1$ to $r_X/s_X \approx 2$. The modelled bulges demonstrate similar values of the sharpness parameter for bars rotated from about 45° to 90° around the disc axis. There are also some galaxies the bulges of which have the parameters that do not fall on the model curves. For example, the bulge in NGC 2654 galaxy has an opening angle value of its X-structure $\varphi \approx 30^\circ$ and a rather small value of the sharpness parameter, $r_X/s_X \approx 0.6$ (the point which is the closest to the bottom left corner of the graph). There is also NGC 5529 galaxy where the X-shaped bulge has $\varphi \approx 36^\circ$ and the sharpness parameter value $r_X/s_X \approx 2$. The corresponding point is the rightmost one. Contrary to the usual train of thoughts, this is rather reassuring that there are some bulges that are not consistent with the modelled bulges in terms of their parameters. This is precisely because we know that our models should not describe all possible cases and especially considering the fact the model curves do not account for the evolution of the B/PS bulges in time. In fact, Fig. 13 encourages us to consider more of different galaxy models at different time moments which we plan to do in future.

Another important observation that we can make from Fig. 17 is the following. The figure shows that we do not detect real B/PS bulges with X-structure angles smaller than those we obtained in the modelled galaxies. Thus, the problem with small opening angles in real galaxies which we encountered in our previous work (Smirnov & Sotnikova 2018) can be considered solved. We can conclude the discrepancy between model and real data which was observed in that work is due to the difference in measuring approaches and there is no need to find some physical reasons for it.

8 SUMMARY AND CONCLUSIONS

Concluding our work, we can state the following:

- (i) We introduced a new photometric model accounting

simultaneously for the boxy/peanut-shaped (B/PS) bulges and the X-structures that reside in such bulges. The functional form of the model is that of a 2D Sersic function with a truncated intensity profile. The truncations are introduced above (in the upper half-plane) and below (in the bottom half-plane) the rays of X-structures. The model allows one to measure the geometric properties of X-structures (opening angle, linear scale) by means of photometric decomposition. We call this new model “the X-shaped bulge model”.

- (ii) The form of the model was deduced based on the appearance of the B/PS bulge in some particular numerical model of the galaxy where such a bulge naturally arises due to the bar thickening. The considered type of numerical model is frequently used to study the secular evolution of early-type SB galaxies. An important aspect of our study is that we first extracted the B/PS bulge using some dynamical considerations. In particular, we split the modelled galaxy into different dynamical subsystems (bar + disc) using the frequency characteristics of particles-“stars”. This allowed us to study the B/PS bulge density distribution in its “pure” form without the need to take into account the disc component when we try to find an appropriate photometric model for the B/PS bulge.

- (iii) Using a set of different galaxy models, we study how the parameters of the X-shaped bulge photometric model vary depending on the projection effects (disc inclination, bar azimuthal viewing angle), the applied photometric model of the disc (a simple exponential disc and an anti-truncated disc) and in case of co-existence of two bulges in the same galaxy. We found that the application of the anti-truncated disc model leads to more reasonable values of the X-shaped bulge parameters than the application of a simple exponential disc model for all disc inclinations and bar orientations considered. In case of the co-existence of two bulges (a B/PS bulge and a classic one), we found that it is indeed possible to retrieve “true” values of the X-shaped bulge parameters even if the bulges are superimposed onto each other.

- (iv) We applied the X-shaped bulge model to study the B/PS bulges of some real galaxies. In total, we considered 29 galaxies. The B/PS bulges of these galaxies were previously studied by Ciambur & Graham (2016), Savchenko et al. (2017) and Laurikainen & Salo (2017) (in each work some sub-sample of our sample) using different methods. For three of these galaxies (NGC 678, NGC 2549, and NGC 4111), we could not obtain a reliable photometric model with the X-shaped bulge component. This is due to the fact that these galaxies did not show a bright X-shape feature when we subtracted Sersic bulge and disc components. We also could not obtain the reliable photometric model for PGC 21357, NGC 3628, and NGC 4469 due to dust feature in these galaxies. For each of the remaining 25 galaxies, we obtained the best-fit photometric model, which includes an X-shaped bulge model as a separate component. We compared the obtained values of opening angles with results of Ciambur & Graham (2016), Savchenko et al. (2017) and Laurikainen & Salo (2017) for the same galaxies. We found that the application of different measuring techniques leads to systematically different results on exactly the same galaxies. On the example of ESO 443-042 galaxy, we showed that 6-th Fourier harmonic amplitude B_6 used by Ciambur & Graham (2016) to characterise B/PS bulges is highly dependent on the disc contribution, and the peanut angle obtained based on it does not correspond to the X-structure opening angle in some cases.

- (v) We compared the geometric characteristics of B/PS bulges of some simulated galaxies with those obtained for real galaxies.

We found that the values are generally consistent with each other if we measure them in exactly the same way for simulated and real galaxies. We found that the real X-structures do not show opening angles smaller than about 27° . Thus, we resolved an inconsistency between the modelled X-structures and the X-structures of real galaxies we encountered in our previous work (Smirnov & Sotnikova 2018). In that work, the X-structures of modelled galaxies showed opening angles on average larger than those of real galaxies. In the present work, we explicitly showed that the difference is due to different approaches to the X-structure measuring.

Concerning future plans, there are two different lines of work we can pursue. First, we did not consider how B/PS bulge parameters evolve with time in the present work, and it is quite an important thing to check since the bars can buckle, and it is possible that using our new model we can capture such a behaviour. We also did not consider how the B/PS bulges of different types of bars, for example, a bar with a barlens or a peanut-shaped bar if viewed face-on, differ in terms of their parameters, which is an interesting thing to check. Two mentioned types were already compared in Laurikainen & Salo (2017) in terms of the B/PS bulges linear sizes but no significant difference was found. Perhaps, using our new model we can reveal some additional differences between these two cases. The second important line is the expansion of the sample of real galaxies and a more thorough comparison of the parameters of real and modelled galaxies.

As a concluding remark, we would like to note the following. The photometric model deduced here is not absolute, in a sense that a more accurate model can be obtained in the future. For example, there can be a model that accounts for the thickness of X-structure rays in an explicit way or the model that somehow traces the bending of its rays. Obviously, the end goal of this road is to find an appropriate 3D bar model, which includes the X-structures as its natural part. The present work can be viewed as the stepping stone on this road.

DATA AVAILABILITY

The data underlying this article will be shared on reasonable request to the corresponding author.

ACKNOWLEDGEMENTS

The authors express gratitude for the grant of the Russian Foundation for Basic Researches number 19-02-00249. AS also thanks N. Ya. Sotnikova and A. A. Marchuk for a helpful discussion of some aspects of this work.

References

Araki S., 1985, PhD thesis, Massachusetts Institute of Technology.
 Athanassoula E., 2005, *MNRAS*, 358, 1477
 Athanassoula E., Laurikainen E., Salo H., Bosma A., 2015, *MNRAS*, 454, 3843
 Bertin E., Arnouts S., 1996, *A&AS*, 117, 393
 Bertin E., Mellier Y., Radovich M., Missonnier G., Didelon P., Morin B., 2002, in Bohlender D. A., Durand D., Handley T. H., eds, *Astronomical Society of the Pacific Conference Series Vol. 281, Astronomical Data Analysis Software and Systems XI*. p. 228
 Bertola F., Capaccioli M., 1977, *ApJ*, 211, 697

Binney J., Petrou M., 1985, *MNRAS*, 214, 449
 Binney J., Spergel D., 1982, *ApJ*, 252, 308
 Burbidge E. M., Burbidge G. R., 1959, *ApJ*, 130, 20
 Bureau M., Freeman K. C., 1999, *AJ*, 118, 126
 Caon N., Capaccioli M., D’Onofrio M., 1993, *MNRAS*, 265, 1013
 Ceverino D., Klypin A., 2007, *MNRAS*, 379, 1155
 Chung A., Bureau M., 2004, *AJ*, 127, 3192
 Ciambur B. C., Graham A. W., 2016, *MNRAS*, 459, 1276
 Combes F., Sanders R. H., 1981, *A&A*, 96, 164
 Combes F., Debbasch F., Friedli D., Pfenniger D., 1990, *A&A*, 233, 82
 D’Onofrio M., Capaccioli M., Merluzzi P., Zaggia S., Boulesteix J., 1999, *A&AS*, 134, 437
 Dehnen W., 2002, *Journal of Computational Physics*, 179, 27
 Eisenstein D. J., et al., 2011, *AJ*, 142, 72
 Erwin P., 2015, *ApJ*, 799, 226
 Erwin P., Debattista V. P., 2013, *MNRAS*, 431, 3060
 Erwin P., Debattista V. P., 2017, *MNRAS*, 468, 2058
 Erwin P., et al., 2015, *MNRAS*, 446, 4039
 Ferrers N. M., 1877, *Quart. J. Pure Appl. Math.*, 14
 Friedli D., Pfenniger D., 1990, in Jarvis B. J., Terndrup D. M., eds, *European Southern Observatory Conference and Workshop Proceedings Vol. 35, European Southern Observatory Conference and Workshop Proceedings*. pp 265–268
 Gajda G., Lokas E. L., Athanassoula E., 2016, *ApJ*, 830, 108
 Hernquist L., 1990, *ApJ*, 356, 359
 Hernquist L., Quinn P. J., 1988, *ApJ*, 331, 682
 Jarvis B. J., 1981, PhD thesis, Australian National University
 Jarvis B. J., 1986, *AJ*, 91, 65
 Kim T., et al., 2014, *ApJ*, 782, 64
 Kormendy J., Barentine J. C., 2010, *ApJ*, 715, L176
 Kormendy J., Illingworth G., 1982, *ApJ*, 256, 460
 Kruk S. J., Erwin P., Debattista V. P., Lintott C., 2019, *MNRAS*, 490, 4721
 Kuijken K., Merrifield M. R., 1995, *ApJ*, 443, L13
 Laurikainen E., Salo H., 2016, in Laurikainen E., Peletier R., Gadotti D., eds, *Astrophysics and Space Science Library Vol. 418, Galactic Bulges*. p. 77 ([arXiv:1505.00590](https://arxiv.org/abs/1505.00590)), doi:10.1007/978-3-319-19378-6_4
 Laurikainen E., Salo H., 2017, *A&A*, 598, A10
 Laurikainen E., Salo H., Athanassoula E., Bosma A., Herrera-Endoqui M., 2014, *MNRAS*, 444, L80
 Lütticke R., Dettmar R.-J., Pohlen M., 2000, *A&AS*, 145, 405
 Makarov D., Prugniel P., Terekhova N., Courtois H., Vauglin I., 2014, *A&A*, 570, A13
 Martín-Navarro I., et al., 2012, *MNRAS*, 427, 1102
 McMillan P. J., Dehnen W., 2007, *MNRAS*, 378, 541
 Merrifield M. R., Kuijken K., 1999, *A&A*, 345, L47
 Merritt D., Sellwood J. A., 1994, *ApJ*, 425, 551
 Navarro J. F., Frenk C. S., White S. D. M., 1996, *ApJ*, 462, 563
 Parul H. D., Smirnov A. A., Sotnikova N. Y., 2020, *ApJ*, 895, 12
 Patsis P. A., Athanassoula E., 2019, *MNRAS*, 490, 2740
 Patsis P. A., Harsoula M., 2018, *A&A*, 612, A114
 Patsis P. A., Katsanikas M., 2014a, *MNRAS*, 445, 3525
 Patsis P. A., Katsanikas M., 2014b, *MNRAS*, 445, 3546
 Patsis P. A., Skokos C., Athanassoula E., 2002, *MNRAS*, 337, 578
 Peterson S. D., 1979, *ApJS*, 40, 527
 Pfenniger D., 1984, *A&A*, 134, 373
 Pfenniger D., Friedli D., 1991, *A&A*, 252, 75
 Poliachenko V. L., Shukhman I. G., 1977, *Soviet Astronomy Letters*, 3, 134
 Portail M., Wegg C., Gerhard O., 2015, *MNRAS*, 450, L66
 Quillen A. C., 2002, *AJ*, 124, 722
 Quillen A. C., Minchev I., Sharma S., Qin Y.-J., Di Matteo P., 2014, *MNRAS*, 437, 1284
 Raha N., Sellwood J. A., James R. A., Kahn F. D., 1991, *Nature*, 352, 411
 Salo H., Laurikainen E., 2017, *ApJ*, 835, 252
 Salo H., et al., 2015, *ApJS*, 219, 4
 Savchenko S. S., Sotnikova N. Y., Mosenkov A. V., Reshetnikov V. P., Bizyaev D. V., 2017, *MNRAS*, 471, 3261
 Schweizer F., Seitzer P., 1988, *ApJ*, 328, 88
 Sellwood J. A., Gerhard O., 2020, *MNRAS*, 495, 3175

- Sersic L. J., 1968, Atlas de Galaxias Australes. Observatorio Astronomico, Cordoba
- Shaw M. A., 1987, [MNRAS](#), **229**, 691
- Sheth K., et al., 2010, [PASP](#), **122**, 1397
- Skokos C., Patsis P. A., Athanassoula E., 2002, [MNRAS](#), **333**, 847
- Smirnov A. A., Sotnikova N. Y., 2018, [MNRAS](#), **481**, 4058
- Teuben P., 1995, in Shaw R. A., Payne H. E., Hayes J. J. E., eds, *Astronomical Society of the Pacific Conference Series Vol. 77, Astronomical Data Analysis Software and Systems IV*. p. 398
- Toomre A., 1966, in *Notes from Geophysical Fluid Dynamics Summer Program. Astrophysics and Space Science Library*. pp 111–114
- Veilleux S., Bland-Hawthorn J., Cecil G., 1999, [AJ](#), **118**, 2108
- Whitmore B. C., Bell M., 1988, [ApJ](#), **324**, 741
- Yoshino A., Yamauchi C., 2015, [MNRAS](#), **446**, 3749
- Zwicky F., Karpowicz M., Kowal C. T., 1965, “Catalogue of Galaxies and of Clusters of Galaxies”, Vol. V
- de Souza R. E., Dos Anjos S., 1987, [A&AS](#), **70**, 465

This paper has been typeset from a $\text{\TeX}/\text{\LaTeX}$ file prepared by the author.